

# Multi-static Parameter Estimation in the Near/Far Field Beam Space for Integrated Sensing and Communication Applications

Saeid K. Dehkordi\*, Lorenzo Pucci<sup>†</sup>, Peter Jung\*, <sup>‡</sup>, Andrea Giorgetti<sup>†</sup>, Enrico Paolini<sup>†</sup>, Giuseppe Caire\*

\*Technical University of Berlin, Germany

<sup>†</sup>Wireless Communications Laboratory, CNIT, DEI, University of Bologna, Italy

<sup>‡</sup>German Aerospace Center (DLR), Germany

Emails: {s.khalilidehkordi, peter.jung, caire}@tu-berlin.de, {lorenzo.pucci3, andrea.giorgetti, e.paolini}@unibo.it

**Abstract**—This work proposes a maximum likelihood (ML)-based parameter estimation framework for a millimeter wave (mmWave) integrated sensing and communication (ISAC) system in a multi-static configuration using energy-efficient hybrid digital-analog arrays. Due to the typically large arrays deployed in the higher frequency bands to mitigate isotropic path loss, such arrays may operate in the near-field regime. The proposed parameter estimation in this work consists of a two-stage estimation process, where the first stage is based on far-field assumptions, and is used to obtain a first estimate of the target parameters. In cases where the target is determined to be in the near-field of the arrays, a second estimation based on near-field assumptions is carried out to obtain more accurate estimates. In particular, we select *beamfocusing* array weights designed to achieve a constant gain over an extended spatial region and re-estimate the target parameters at the receivers. We evaluate the effectiveness of the proposed framework in numerous scenarios through numerical simulations and demonstrate the impact of the custom-designed flat-gain beamfocusing codewords in increasing the communication performance of the system.

**Index Terms**—integrated sensing and communication, OFDM, near field parameter estimation, multi-static ISAC.

## I. INTRODUCTION

In the context of 5G and beyond wireless systems, integrated sensing and communication (ISAC) has emerged as one of the key components [1]. Contrary to the active localization already existing in mobile systems, where the user equipments (UEs) interact with the Base Stations (BSs) for position estimation, the idea behind ISAC systems is that of having a wireless communication network composed of one or more BSs, able to localize passive objects present in the environment only by collecting and analyzing the signal reflected by them, thus using the same hardware resources and the same physical layer used for communication, allowing more efficient use of the spectrum. Incorporating sensing into next-generation mobile systems unlocks vast capabilities for applications like traffic monitoring, pedestrian detection, and urban autonomous driving [2]. Recent studies have demonstrated the potential of employing orthogonal frequency division multiplexing (OFDM)-based waveforms for ISAC systems, with a focus in particular on the mono-static configuration, that is, with the transmitter (Tx) and receiver (Rx) co-located [3], [4], [5].

However, this configuration requires extra hardware or digital processing to remove self-interference [4].

A possible solution to avoid the self-interference problem is to resort to a bi-static configuration, where the Tx and Rx are not co-located. Bi-static radar setups are also interesting in that they can extend the sensing area with cost-effective Rx units, which may also be mobile [6]. For these reasons, bi-static and multi-static ISAC configurations are attracting increasing amounts of interest for future 5th generation and beyond (5G) networks [7], [8]. In order to achieve the required level of delay and angle resolution, radar sensing requires large antenna arrays and wideband signals. Communication waveforms (such as OFDM) in 5G are expected to use high frequencies (28 — 100 GHz) and large signal bandwidths. Due to the small wavelength, large arrays can be implemented in relatively small form factors. However, the implementation of fully digital architectures becomes extremely challenging due to the enormous data rate of the A/D conversion at each antenna element. In order to alleviate this problem, hybrid digital-analog (HDA) architectures are commonly considered for massive multiple-input multiple-output (MIMO) communications.

Another interesting aspect connected to the use of very large arrays is that, for some users and radar targets, the usual far-field (FF) assumption common to most array processing literature is not satisfied any longer [9]. In the case of near-field (NF) propagation, the usual modeling of the received signal as a superposition of planar waves impinging on the array from multiple scattering elements is not valid, and NF-specific algorithm design for communication and sensing is required.

While most of the available literature focuses on the two extreme cases (either the FF or NF regime [10]) for the algorithmic design of ISAC systems, to the best of the authors' knowledge, the state-of-the-art still lacks studies on the sensing and communication performance of a multi-static (or bi-static) ISAC system, taking into account both NF and FF scenarios. In order to employ a beamforming/beamfocusing scheme adapted to the propagation scenario, it is necessary to determine whether the radar target (or the UE) is in FF or NF conditions.

This requires some initial estimation, that is agnostic of the propagation conditions. For this reason, this work considers a multi-static ISAC configuration composed of two bi-static pairs, capable of detecting and localizing extended sensing objects that are located in the NF or FF of the Tx and/or one of the Rx without a priori knowledge.

Motivated by the lower dimensionality of the beamforming codebook and the reduced parameter search space of the FF model, the proposed framework *initializes* the sensing operation in the beam-space by using FF beamforming vectors and performing maximum likelihood (ML) detection and estimation. Based on the target estimation obtained from this initial stage of sensing, the strategy for the second stage is determined. If the presence of targets in the NF of the Tx is detected, the scheme switches the Tx beamforming to a beamfocusing approach, thus increasing the signal-to-noise ratio (SNR) at the intended target (UE) location. To obtain the beamfocusing weights, a beam-focusing codebook at Tx is utilized where the codewords are designed to maintain an (almost-) constant gain within an extended spatial region. In the communication-only context, requiring some active scheme between the BS and UE, two-step processes for designing beamformers/beamfocusing have also been advocated in other works (e.g. [11]). Considering the possibility that the detected target may be a communication user, the ability to appropriately illuminate it can lead to a significant increase in the SNR and thus an increase in communication performance (i.e. spectral efficiency). In accordance with [12], [11], our numerical results show that the beamfocusing scheme converges to beamforming within the transitional region of the NF and FF.

If the target is detected to be in FF of both the Tx and Rx arrays, a second stage is not required. Nevertheless, as shown in our previous work [5], with adequately accurate positional estimates, it is possible to switch to FF beamformers with higher directivity to increase the operating SNR. If the target is determined to be in NF of an Rx array, since the FF model used in the first stage is mismatched, the second stage performs another ML estimation of the target parameters with the correct NF model, resulting in significantly improved estimation performance.

The main contributions of this work are highlighted in the following:

- We consider a multi-static ISAC system, composed of one Tx and two Rx's, capable of exploiting the spatial diversity, i.e. the view of the target from different perspectives, to obtain an accurate estimate of extended targets in the system coverage area. Additionally, the setup in this work is based on HDA architectures which have been shown to be energy and cost-efficient.
- We provide a general model, valid for both NF and FF channel conditions, that accounts for amplitude and phase variations at different antenna elements in the NF and converges to the well-known line-of-sight (LoS) propagation model in the FF.

- We propose a two-stage parameter estimation framework that is generalized to the location of the target with regards to being located in the NF or FF of the multi-static deployment topology.
- For cases when a target (UE) is determined to be in the NF of the Tx, we introduce a novel algorithm to create a beamfocusing codebook that maintains a constant gain over an extended spatial region. We then demonstrate that it is possible to drastically improve the localization and communication performance by using beam focusing instead of beamforming.
- Given that one of the main advantages of multi-static radar setups is to increase system robustness in terms of target detection, we show via numerical examples that by fusing the information from the two Rx's, it is possible to significantly increase target detection performance.

We adopt the following notations:  $(\cdot)^*$  and  $(\cdot)^T$  denote the complex conjugate and transpose operations, respectively, while  $(\cdot)^H$  denotes the Hermitian (conjugate and transpose) operation.  $|x|$  denotes the absolute value of  $x$  if  $x \in \mathbb{R}$ , while  $|\mathcal{X}|$  denotes the cardinality of a set  $\mathcal{X}$ .  $\|\mathbf{x}\|_2$  denotes the  $\ell_2$ -norm of a complex or real vector  $\mathbf{x}$ .  $\mathbf{I}_m$  denotes the  $m \times m$  identity matrix. We let  $[n] = \{1, \dots, n\}$  and  $[0 : n] = \{0, 1, \dots, n\}$  for a positive integer  $n$ .  $\otimes$  denotes Kronecker product.

The rest of the paper is organized as follows. In Section II, the considered extended target model, the near/far field region relationship, and the generalized near/far field channel model are given, while in Section III the OFDM input-output relationship for a single bi-static system in the presence of reflections from extended targets is provided. In Section IV ML estimator is derived and our two-stage parameter estimation framework is presented. Section V introduces a novel algorithm that generates a beamfocusing codebook, ensuring a consistent gain across an extended spatial area. Numerical results are presented in Section VI, and Section VII concludes the paper with some remarks.

## II. SYSTEM MODEL

In this paper, a multi-static ISAC configuration is considered. In particular, as shown in Fig. 4, the system consists of a Tx and two Rx units to form two bi-static Tx-Rx pairs. By using multiple Rx's, it is possible to see the targets from different perspectives, thus providing a diversity gain, especially in the case of extended targets. In fact, a well-known advantage of bi-static/multi-static sensing configurations is to provide an enhanced radar cross section (RCS) based observation of targets (i.e., compared to the mono-static configuration), since different observation perspectives of targets result in different measurements [13]. Another advantage of bi-static setup is that full-duplex processing which would otherwise be required for mono-static sensors is not necessary <sup>1</sup>. As in most of the related literature, we assume that a connection between the Tx

<sup>1</sup>Full-duplex operations can be achieved with sufficient isolation between the transmitter and the radar receiver [14], [15], nevertheless are still considered a challenge.

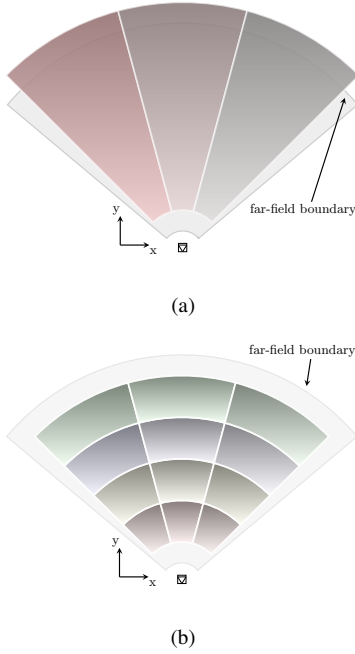


Fig. 1: Schematic representation of a codebook of (a) beamforming and (b) beamfocusing codewords in the spatial domain. Note that the FF beamformers extend beyond the Fraunhofer distance and beamfocusing codewords are designed to cover only up to the Fraunhofer distance (i.e. NF region). Additionally, the codewords do not need to uniformly divide the space. As an example, in typical urban deployments, areas with more densely located users can be assigned more refined codewords and vice versa.

and Rx units via either a *wired* backhaul or wireless radio link is established.

In our analysis, we consider OFDM as the modulation scheme since it is considered one of the standardized waveforms for 5G-NR millimeter wave (mmWave) systems and ISAC applications<sup>2</sup> [16]. In particular, to accomplish the sensing task, we consider that the Tx transmits a frame consisting of  $N$  OFDM symbols, for a duration equal to  $NT_0$ , where  $T_0 \triangleq 1/\Delta f + T_{cp}$  is the total OFDM symbol duration including the cyclic prefix, and with a bandwidth of  $W = M\Delta f$ , where  $M$  is the total number of subcarriers and  $\Delta f$  is the subcarrier spacing. The system operates over a channel with carrier frequency  $f_c \gg W$ , such that the narrowband array response assumptions hold [17]. The generic subcarrier has the frequency  $f_m = f_c + m\Delta f$ , where  $m = -M/2, \dots, M/2 - 1$ . Aiming at hardware cost and energy efficiency, we consider a *fully-connected* HDA array architecture (see e.g. [18]) where the BS transmitter is equipped with  $N_{rf}$  Tx radio frequency (RF) chains driving an antenna array with  $N_{tx}$  elements. The radar receivers have the same architecture as the BS.

For communication, the BS transmits  $1 \leq Q \leq N_{rf}$

<sup>2</sup>Note that the analysis performed is general and remains valid even if a different multi-carrier modulation scheme is chosen, such as orthogonal time frequency space (OTFS).

data streams through a beamforming matrix  $\mathbf{F} = [\mathbf{f}_1, \dots, \mathbf{f}_Q]$  where  $\mathbf{f}_q$  denotes the  $q$ -th column of  $\mathbf{F}$  associated to the  $q$ -th data stream. The design of Tx beamformers  $\mathbf{f}_q$  involves ensuring that each covers a relatively wide section of the beam space with a constant gain, and maintains a very low gain elsewhere (see [5] for detailed information). In particular, the Tx beamforming vectors are such that  $\mathbf{f}_q^H \mathbf{f}_{q'} \approx 0$ , for all  $q' \neq q$ . Subsequently, the backscattered signal originating from the targets (or UEs) within the beam space segment covered by the respective Tx beamforming vectors is utilized for radar processing. It is worth noting that our aim in estimating accurately the UEs parameters is to eliminate the necessity for active localization feedback in the uplink communication.

In this work, we assume the number of legitimate targets (i.e. users) is known via communication between the user devices and the BS, here serving as the host radar. In this context, the beamforming codewords are selected such that each codeword only covers a single target in the beam space. Therefore, we focus on a scenario where a single data stream (i.e.,  $\mathbf{F} = \mathbf{f}$ ) is directed towards the UE within a specific sector.

*Remark 1.* In this study, in addition to the beamforming codebook used for the FF beamforming, the second stage of the scheme comprises *beamfocusing* codewords for transmission in the NF. The above assumptions of separated extended targets in the FF beam space will be preserved for the NF case, where the Tx beamfocusing codewords are designed to be non-overlapping and illuminate only a single extended target.

The mmWave systems considered for 5G NR and beyond communications are expected to operate under *codebook*-based schemes (e.g. as defined in TS 38.214 [19]). A wide variety of codebook-based schemes have been proposed and investigated in literature (see [20], [21] and refs therein). This work focuses on the estimation of the spatial parameters of extended-targets (ETs) that are located in a sensing area (Fig. 4) resembling an urban deployment. Given that our approach operates on a codebook basis, we adopt a time division operation mode. In this mode, a beamforming (BF) codeword of the Tx is selected, and the receivers scan the portion of the beam space illuminated by the respective Tx beamformer. Consequently, parameter estimation is carried out specifically within this beam space sector. This process continues sequentially until the entire desired beam space region has been covered. The HDA architecture does not allow conventional MIMO radar processing, and a vector observation of the beam space (i.e. multiple samples of the beam space) is required for angle estimation. To address this, we define a codebook containing a set of  $N_a$  discrete Fourier transform (DFT) orthogonal beams as  $\mathcal{U}_{\text{DFT}} := (\mathbf{u}_1, \dots, \mathbf{u}_{N_a}) \in \mathbb{C}^{N_a \times N_a}$  selected from the Fourier basis ( $\in \mathbb{C}^{N_a \times N_a}$ ), where  $N_a$  is the number of antenna array elements. Subsequently,  $N_{rf}$  beams out of the  $N_a$  are selected at Rx units, ensuring coverage of a desired region of interest in the beam space (i.e., covering the illuminated region by the Tx) resulting in the formation of the reduction matrix  $\mathbf{U} \in \mathbb{C}^{N_a \times N_{rf}}$ . In scenarios where

more than  $N_{\text{rf}}$  beams are required to span the illuminated spatial segment, a multi-block-measurement scheme can be adopted (see [5], [22] for details). Such a scheme can easily be justified as a result of minimal target movement over the interval  $B$  OFDM blocks required for signal acquisition, where  $B$  is typically small.

*Remark 2.* The HDA system model in this work can be readily transformed into a fully-digital system. In this case,  $N_{\text{rf}} = N_{\text{a}}$  RF chains are used to demodulate and sample all the antennas of the radar Rx, thus allowing full digital processing.

### A. Target model

It is common practice to represent an extended target as a set of fixed point-scatterers. As an alternative approach, it is possible to produce a measurement model (likelihood) in terms of the spatial density of measurements in the intended sensing area. Specifically, motivated by finite element discretization techniques commonly used for RCS characterization [23], in this work, the target is modeled as a set of grid elements  $\mathcal{P}$  within a designated rectangular region  $\mathbf{A} \subset \mathbb{R}^2$  with an area of  $|\mathbf{A}|$ , as shown in Fig. 2. At each instant the radar measurement is made, the extended target representing a UE (e.g., vehicle, motorcycle, etc.) is composed of a random number  $P \leq |\mathcal{P}|$  of scatterers. Given that each grid point inside  $\mathbf{A}$  can be active with probability  $q$ , the number of active points  $P$  follows a binomial distribution (BND), with probability  $q$  and number of trials  $|\mathcal{P}|$ , i.e.,  $P \sim \text{B}(q, |\mathcal{P}|)$ . Then, the probability of having  $p$  active points at each instant is given by the probability mass function<sup>3</sup>:

$$\Pr(P = p) = \binom{|\mathcal{P}|}{p} q^p (1 - q)^{|\mathcal{P}| - p}.$$

Then,  $P$  points (elements) are drawn i.i.d. from  $\mathcal{P}$  such that  $P \subseteq \mathcal{P}$ .

In the considered channel model, each individual scattering point (represented by an element) is characterized only by its LoS path since mmWave channels are characterized by large isotropic attenuation, so multipath components are typically much weaker than the LoS and disappear below the noise floor after reflection, especially for the scattering channel seen by the radar receiver (see, e.g., [24], [25]). With an appropriate choice of grid size, the variable number of scatterers in the target area can be used to model the fluctuations and variance of radar reflectivity of an object caused by target aspect angle, material, etc.

Since in this work, we consider a multi-static system, the reflection points observed by each RX unit are generated by a separate BND process at each measurement instance.

### B. Near/far-field region relationship

The boundary between NF and FF can be determined by the *Fraunhofer* distance (also called Rayleigh distance). For

<sup>3</sup>Interesting to note that, considering a finite but very large number of elements on the grid, i.e.  $|\mathcal{P}| \rightarrow \infty$ , each of which is independent active or non-active, the binomial distribution can also be very well approximated by a Poisson distribution, with intensity  $\gamma = q|\mathcal{P}|$ .

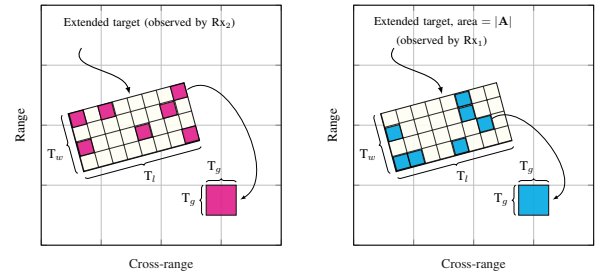


Fig. 2: Schematic of the target model, composed of scattering point clusters determined through a BND. Note that each Rx observes a different scattering profile of the extended target at each measurement instance. The parameter values are provided in Tab. II.

an antenna with maximum aperture  $D$  at wavelength  $\lambda$ , the Fraunhofer distance given by  $D_{\text{ff}} = \frac{2D^2}{\lambda}$  represents the minimum distance for guaranteeing the phase difference of received signals across the array elements of at most  $\lambda/4$  [9]. For a uniform linear array (ULA) with  $N_{\text{a}}$  elements and  $\lambda/2$  inter-element spacings, this equates to  $N_{\text{a}}^2 \lambda/2$ . This is widely considered the limit under which wave propagation under the planar assumption holds. The Fresnel distance  $D_{\text{fr}}$  given by  $\sqrt[3]{\frac{D^4}{8\lambda}}$  is the distance beyond which the reactive field components of the antenna itself become negligible. The distance between  $D_{\text{ff}}$  and  $D_{\text{fr}}$  is of interest in this work (see Fig. 4), which is known as the radiative NF Fresnel region, or the NF region for brevity.

*Remark 3.* An important note is in order. When dealing with multi-band systems, the Fraunhofer distance is impacted by the wavelength of each component. More specifically, for the OFDM format considered in this work, the Fraunhofer distance varies for each sub-carrier. The overall FF regime of the system with a fixed array aperture can then be considered as the Fraunhofer distance of the highest frequency sub-carrier, i.e.  $D_{\text{ff}} = 2D^2 / \min(\lambda_m)$ . Figure 3 depicts  $D_{\text{ff}}$  for a few mmWave carrier frequencies and bandwidths where the number of OFDM subcarriers is  $M = 100$ . As observed, for the system parameters selected in Section VI, the small bandwidth leads to approximately the same  $D_{\text{ff}}$  across all subcarriers. Nonetheless, for critical cases, this has to be taken into account and the processing needs to be carried out on a per sub-carrier basis separately.

### C. Channel model

The considered ISAC system can operate in both NF and FF. In contrast to the FF channel model where the signal wavefront is approximated to be a plane, the NF channel is modeled to account for a spherical wavefront. This generates a substantial difference between the two regimes. In fact, in FF processing, the angle and distance of the target are estimated based on the array response and the time delay of the signal, independently, where the time delay resolution is limited by the system bandwidth. In contrast, in the NF regime, it is possible to directly localize the target without estimating time delay, but only by analyzing the phase of the signal scattered



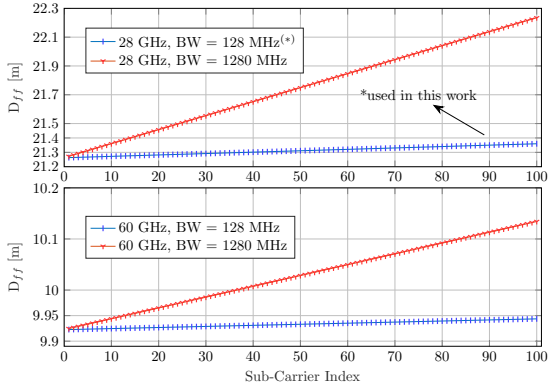


Fig. 3: FF distance as a function of OFDM sub-carrier index.

by the target and acquired by different antenna array elements, by exploiting the properties of a spherical wave. However, a general channel model can be found that is valid for both scenarios, i.e. that provides an acceptable approximation in the NF and converges as a limit case to the well-known FF model as the distance between the target and Tx/Rx increases.

For simplicity, we consider for a while a single scatterer  $p$  (taken from a generic extended target  $l$ ) located at  $\mathbf{p}_p$  and a transmitting antenna array  $k$  whose  $N_{\text{tx}}$  elements are located at  $\mathbf{p}_{k_i}$ , with index  $i = -\frac{N_{\text{tx}}-1}{2}, \dots, \frac{N_{\text{tx}}-1}{2}$ , and an inter-element spacing of  $d$ . Considering LoS propagation conditions, the equivalent low-pass complex channel coefficient for the channel between the single antenna element  $k_i$  and the scatterer  $p$  at subcarrier  $m$  and time  $n$  can be written as

$$\eta_{k_i,p}^{(m,n)} = \sqrt{\xi_{k_i,p}} e^{-j\varphi_{k_i,p}^{(m)}} e^{j2\pi n T_0 \nu_{k,p}} \quad (1)$$

where  $\nu_{k,p}$  is the Doppler shift,  $\varphi_{k_i,p}^{(m)}$  is the phase term given by

$$\varphi_{k_i,p}^{(m)} = 2\pi \frac{r_{k_i,p}}{c} f_m + \varphi_0, \quad (2)$$

and  $\xi_{k_i,p}$  is the gain factor of the channel between the antenna  $k_i$  and the scatterer  $p$ , which, considering LoS propagation conditions, can be written as follows

$$\xi_{k_i,p} = \frac{\sigma_{k,p}}{4\pi r_{k_i,p}^2} \quad (3)$$

with  $r_{k_i,p} = \|\mathbf{p}_p - \mathbf{p}_{k_i}\|$  the distance between the  $k_i$ th antenna of the Tx and the scatterer  $p$ ,  $c$  is the speed of light,  $\varphi_0 \in \mathcal{U}_{[0,2\pi)}$  is the phase offset between Tx and Rx, and  $\sigma_{k,p}$  the RCS of the scatterer  $p$ , illuminated by the Tx  $k$ .

As previously stated, the expression in (1) is general and remains valid for both FF and NF scenarios. Later it will be shown that with some approximations resulting by considering the array size much less than  $r_{k,p}$ , which is the distance between the center of the transmitting array  $k$ th (chosen as the reference point) and the scatterer  $p$ , and the same amplitude at each antenna element of the array, (1) can be simplified in the FF. To better highlight the generality of the model, (2) can be rewritten as

$$\varphi_{k_i,p}^{(m)} = 2\pi \frac{r_{k,p}}{c} f_m + 2\pi \frac{r_{k_i,p} - r_{k,p}}{c} f_m + \varphi_0 \quad (4)$$

and as a result, (1) becomes

$$\begin{aligned} \eta_{k_i,p}^{(m,n)} &= \sqrt{\xi_{k_i,p}} e^{-j \left( 2\pi \frac{r_{k_i,p}}{c} (f_c + m\Delta f) + 2\pi \frac{r_{k_i,p} - r_{k,p}}{c} f_m + 2\pi n T_0 \nu_{k,p} + \varphi_0 \right)}. \end{aligned} \quad (5)$$

From (5) the channel vector  $\boldsymbol{\eta}_{k,p}^{(m,n)} \in \mathbb{C}^{1 \times N_{\text{tx}}}$  associated with subcarrier  $m$  and scatterer  $p$  at time  $n$ , can be obtained as:

$$\boldsymbol{\eta}_{k,p}^{(m,n)} = \alpha_{k,p} e^{j2\pi(nT_0\nu_{k,p} - m\Delta f\tau_{k,p})} \mathbf{a}^H(\phi_{k,p}, r_{k,p}) \quad (6)$$

where  $\alpha_{k,p} = \sqrt{\xi_{k,p}} e^{-j(2\pi f_c \tau_{k,p} + \varphi_0)}$  is the reference channel coefficient computed with respect to the center of the antenna array, with  $\tau_{k,p} = r_{k,p}/c$  the reference propagation delay and  $\xi_{k,p}$  the reference channel gain, while  $\mathbf{a}(\phi_{k,p}, r_{k,p}) \in \mathbb{C}^{N_{\text{tx}} \times 1}$ , is the array response vector, computed considering  $W \ll f_c$ , and defined as:

$$\mathbf{a}(\phi_{k,p}, r_{k,p}) = \begin{pmatrix} \frac{r_{k,p}}{r_{0,p}} \exp\left(-j \frac{2\pi f_c}{c} (r_{0,p} - r_{k,p})\right) \\ \frac{r_{k,p}}{r_{1,p}} \exp\left(-j \frac{2\pi f_c}{c} (r_{1,p} - r_{k,p})\right) \\ \vdots \\ \frac{r_{k,p}}{r_{N_{\text{tx}}-1,l}} \exp\left(-j \frac{2\pi f_c}{c} (r_{N_{\text{tx}}-1,l} - r_{k,p})\right) \end{pmatrix}. \quad (7)$$

The relationship between the reference distance  $r_{k,p}$  and the distance of the  $k_i$ th antenna element from the scatterer  $p$  can be obtained from a second order Taylor expansion, considering  $\mathbf{p}_p = r_{k,p}[\cos \phi_{k,p}, \sin \phi_{k,p}]^T$  and  $\mathbf{p}_{k_i} = [0, id]^T$ , as follows

$$r_{k_i,p} - r_{k,p} \approx \frac{(id \cos \phi_{k,p})^2}{2r_{k,p}} - id \sin \phi_{k,p} \quad (8)$$

where  $\phi_{k,p}$  is the reference angle of departure (AoD) related to the scatterer  $p$ . By replacing (8) in (7) and considering  $id \ll r_{k,p} \forall i$ , and  $r_{k,p}/r_{k_i,p} \approx 1$  as reasonable assumptions in the FF, the array response vector in (7) when  $d = c/(2f_c)$ , (7) can be rewritten as

$$\mathbf{a}(\phi_{k,p}) = [e^{-j \frac{N_{\text{tx}}-1}{2} \pi \sin \phi_{k,p}}, \dots, e^{j \frac{N_{\text{tx}}-1}{2} \pi \sin \phi_{k,p}}]^T. \quad (9)$$

The channel between a given scatterer  $p$  and a Rx unit  $j$ , consisting of  $N_{\text{rx}}$  antenna elements can be modeled in the same way as the one between Tx and the scatterer. The only difference is in the channel gain coefficient, as shown below. In particular, the channel vector  $\boldsymbol{\eta}_{p,j}^{(m,n)} \in \mathbb{C}^{N_{\text{rx}} \times 1}$  related to the  $m$ -th subcarrier and  $n$ -th time instant is given by

$$\boldsymbol{\eta}_{p,j}^{(m,n)} = \beta_{p,j} e^{j2\pi(nT_0\nu_{p,j} - m\Delta f\tau_{p,j})} \mathbf{b}(\theta_{p,j}, \gamma_{p,j}) \quad (10)$$

where  $\beta_{p,j} = \sqrt{\zeta_{p,j}} e^{-j2\pi f_c \tau_{p,j}}$  is the reference channel coefficient computed with respect to the center of the  $j$ -th receiving antenna array, and  $\tau_{p,j} = \gamma_{p,j}/c$  the reference propagation delay with  $\gamma_{p,j}$  is the distance between scatterer  $p$  and the center of antenna array  $p$ , and  $\zeta_{p,j}$  the reference channel gain, while  $\mathbf{b}(\theta_{p,j}, \gamma_{p,j}) \in \mathbb{C}^{N_{\text{rx}} \times 1}$  is the array response vector computed as in (7), with  $\theta_{p,j}$  the reference angle of arrival (AoA). The gain factor  $\zeta_{p,j}$ , considering LoS propagation

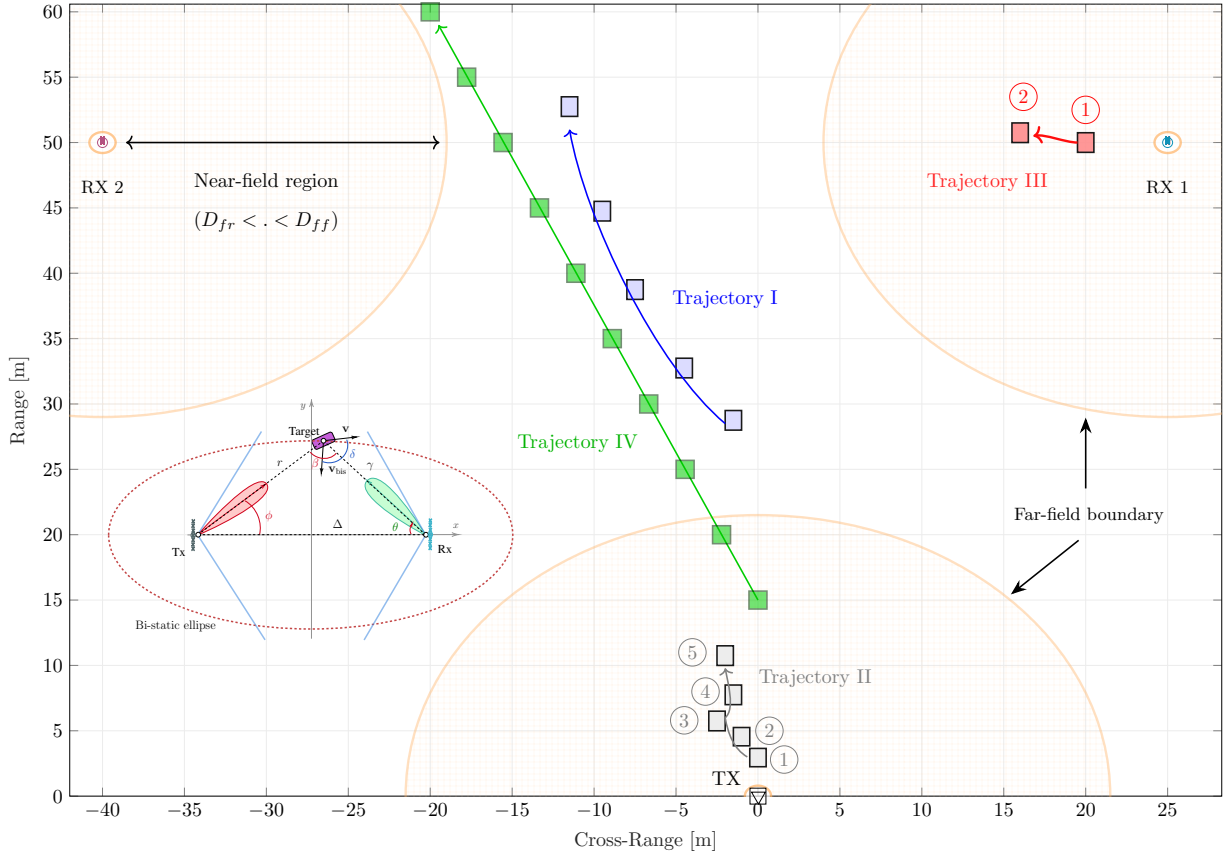


Fig. 4: System topology resembling an urban deployment scenario. The trajectories indicated in the figure model various locations and movement patterns that may arise with respect to the near and far fields of the antenna arrays. We assume that the deployment has been planned such that the NFs of the Tx/Rx pairs do not coincide. The inset depicts the geometric relation between a Tx/Rx pair and the bi-static ellipse described in Section IV-B.

conditions and isotropic antenna elements with effective area  $A = c^2/(4\pi f_c^2)$ , can be written as

$$\zeta_{p,j} = \frac{c^2}{(4\pi f_c \gamma_{p,j})^2}. \quad (11)$$

Now, we consider a generic extended target  $l$ , which is modeled as a group of independent scatterers generated according to a BND, as described in Section II-A. Each of the Tx-Rx bi-static pairs with index  $(k, j)$  can collect echoes from a random set  $P_{k,j}^{(l)} \subseteq \mathcal{P}$  of these points.<sup>4</sup> The  $1 \times N_{\text{tx}}$  time-varying channel between a generic Tx  $k$  and a scatterer point  $p \in [P_{k,j}]$  is given by<sup>5</sup>

$$\mathbf{h}_{k,p}(t) = \alpha_{k,p} \delta(t - \tau_{k,p}) \mathbf{a}^H(\phi_{k,p}, r_{k,p}) \quad (12)$$

where  $\mathbf{a}(\phi_{k,p}, r_{k,p}) \in \mathbb{C}^{N_{\text{tx}} \times 1}$  is the array response vector associated to the scatterer  $p$ , defined as in (7), and  $\delta(\cdot)$  is the Dirac delta function.

<sup>4</sup>In the following, for notation brevity, we indicate with  $P = |P_{k,j}^{(l)}|$  the random number of scatterers related to target  $l$ .

<sup>5</sup>Note that in the considered time-varying channel models, the Doppler shift term is ignored for ease of notation and will be reintroduced into the model later.

Similarly, the  $N_{\text{rx}} \times 1$  time-varying channel between a generic Rx  $j$  and a scatterer point  $p$  is given by

$$\mathbf{h}_{p,j}(t) = \beta_{p,j} \delta(t - \tau_{p,j}) \mathbf{b}(\theta_{p,j}, \gamma_{p,j}). \quad (13)$$

Next, considering (12) and (13) and a bi-static pair  $(k, j)$ , the  $P \times N_{\text{tx}}$  channel between the Tx  $k$  and the target  $l$ , and the  $N_{\text{rx}} \times P$  channel between the Rx  $j$  and the target  $l$ , can be written as

$$\mathbf{H}_{k,l}(t) = [\mathbf{h}_{k,1}^T(t), \dots, \mathbf{h}_{k,P}^T(t)]^T \quad (14)$$

$$\mathbf{H}_{l,j}(t) = [\mathbf{h}_{1,j}(t), \dots, \mathbf{h}_{P,j}(t)] \quad (15)$$

respectively.

The  $N_{\text{rx}} \times N_{\text{tx}}$  time-varying MIMO channel can be obtained as the convolution of the two downlink channels in (14) and (15), and is given by

$$\begin{aligned} \mathbf{H}_{k,j}(t) &= \mathbf{H}_{l,j}(t) * \mathbf{H}_{k,l}(t) \\ &= \sum_{p=1}^P \varepsilon_p \mathbf{b}(\theta_{p,j}, \gamma_{p,j}) \mathbf{a}^H(\phi_{k,p}, r_{k,p}) \delta(t - \tau_p) \end{aligned} \quad (16)$$

where  $\varepsilon_p = \alpha_{k,p} \beta_{p,j}$  is the bi-static complex attenuation factor,  $\tau_p = \tau_{k,p} + \tau_{p,j}$  is the bi-static propagation delay associated with the  $p$ -th scatterer of the target.

### III. OFDM INPUT-OUTPUT RELATIONSHIP

The OFDM frame transmitted from Tx  $k$  to target  $l$  is given by

$$\mathbf{s}_{k,l}(t) = \mathbf{f}_l \sum_{n=0}^{N-1} \sum_{m=0}^{M-1} x_{k,l}[m, n] g_{m,n}(t) \quad (17)$$

where  $\mathbf{f}_l \in \mathbb{C}^{N_{\text{tx}} \times 1}$  is a (unit-norm) transmit beamforming (in the FF) or beamfocusing (in the NF) vector to point toward  $l$ , and  $x_{k,l}[m, n]$  is a generic complex modulation symbol of the  $M \times N$  OFDM resource grid used at the Tx  $k$  to estimate range, angle, and velocity parameters of the target  $l$ ;  $g_{m,n}(t)$  is given by

$$g_{m,n}(t) = \text{rect}\left(\frac{t - nT_0}{T_0}\right) e^{j2\pi m \Delta f (t - T_{\text{cp}} - nT_0)} \quad (18)$$

where  $\text{rect}(x)$  is a pulse-shaping function taking value 1 when  $0 \leq x \leq 1$  and 0 elsewhere.

Next, given the convolution between the time-varying MIMO channel in (16) and the transmitted signal in (17), the noise-free  $N_{\text{rx}}$ -dimensional continuous-time signal transmitted by  $i$  Tx, scattered by the extended target, and received from the  $j$ th Rx is given by

$$\begin{aligned} \mathbf{r}_{k,j}(t) &= \sum_{p=1}^P \varepsilon_p \mathbf{b}(\theta_{p,j}, \gamma_{p,j}) \mathbf{a}^H(\phi_{k,p}, r_{k,p}) \mathbf{s}_{k,l}(t - \tau_p) \\ &= \sum_{p=1}^P \varepsilon_p \mathbf{b}(\theta_{p,j}, \gamma_{p,j}) \mathbf{a}^H(\phi_{k,p}, r_{k,p}) \cdot \\ &\quad \mathbf{f}_l \sum_{n=0}^{N-1} \sum_{m=0}^{M-1} x_{k,l}[m, n] g_{m,n}(t - \tau_p). \end{aligned} \quad (19)$$

As previously mentioned, the Tx beamformers/beamfocusers are designed to cover non-overlapping sections in the beam space. In the simultaneous presence of multiple (extended) targets we place an assumption that the  $L$  (extended) targets are sufficiently separated in space, i.e.,  $|\mathbf{a}^H(\phi_{k,l}, r_{k,l}) \mathbf{f}_{l'}(\hat{\phi}_{k,l'}, \hat{r}_{k,l'})| \approx 0$  for  $l' \neq l$ , where  $\hat{\phi}_{k,l'}$  is the pointing direction (AoD) for a Tx beamformer  $\mathbf{f}_{l'}$  associated with the  $l'$ th (extended) target.

In the following, we focus on using a single Tx beamformer such that multiple segments of the beam space are served in TDM fashion. Aiming at reducing hardware complexity and energy consumption at the radar receiver, we process the received signal  $\mathbf{r}_{k,j}(t)$  by a reduction matrix before sampling. In particular, we focus the radar receiver on a single target  $l$  for  $B$  OFDM frames and estimate different targets sequentially in time. To achieve this, a reduction matrix  $\mathbf{U}_b \in \mathbb{C}^{N_{\text{rx}} \times N_{\text{rx}}^{\text{rf}}}$  is chosen to cover a particular area in the beam space (determined by the current Tx beamformer). Then, after the OFDM demodulator, considering negligible inter-carrier interference (ICI) and inter-symbol interference (ISI) and including noise, a received time-frequency grid of complex elements  $y[m, n]$  is obtained at each RF chain. The expression of the bi-static wireless channel between Tx  $k$  and Rx  $j$ , which is the DFT

sample of (16) at  $m$ -th subcarrier and  $n$ -th time instant, can be easily obtained as the outer product between the  $N_{\text{rx}} \times 1$  channel vector in (10) and the  $1 \times N_{\text{tx}}$  channel vector in (6), as follows

$$\begin{aligned} \mathbf{H}_{k,j}^{(m,n)} &= \sum_{p=1}^P \boldsymbol{\eta}_{p,j} \boldsymbol{\eta}_{k,p} \\ &= \sum_{p=1}^P \varepsilon_p e^{j2\pi(nT_0 \nu_p - m \Delta f \tau_p)} \mathbf{b}(\theta_{p,j}, \gamma_{p,j}) \mathbf{a}^H(\phi_{k,p}, r_{k,p}) \end{aligned} \quad (20)$$

where  $\nu_p = \nu_{k,p} + \nu_{p,j}$  is the bistatic Doppler shift related to  $p$ th scatterer, whose expression will be given in Section IV-B. Thus, the  $N_{\text{rx}}^{\text{rf}} \times 1$  vector of the received complex modulation symbols for a specific block  $b$  is given by

$$\begin{aligned} \mathbf{y}_b[m, n] &= \sum_{p=1}^P \varepsilon_p \mathbf{U}_b^H \mathbf{b}(\theta_{p,j}, \gamma_{p,j}) \mathbf{a}^H(\phi_{k,p}, r_{k,p}) \\ &\quad \mathbf{f}_l x_{k,l}[m, n] e^{j2\pi(nT_0 \nu_p - m \Delta f \tau_p)} + \mathbf{w}[m, n]. \end{aligned} \quad (21)$$

where  $\mathbf{w} \sim \mathcal{CN}(\mathbf{0}, \sigma_w^2 \mathbf{I}_{N_{\text{rx}}^{\text{rf}}})$  is the complex Gaussian noise. By stacking the  $M \times N$  OFDM symbol grid into a  $MN \times 1$  vector  $\underline{\mathbf{x}}_b$ , where the underline symbol indicates blocked quantities, and defining  $\mathbf{T}(\tau, \nu) \in \mathbb{C}^{NM \times NM}$  as

$$\begin{aligned} \mathbf{T}(\tau, \nu) &= \text{diag}([1, \dots, e^{j2\pi n T_0 \nu}, \dots, e^{j2\pi(N-1)T_0 \nu}]^T \\ &\quad \otimes [1, \dots, e^{-j2\pi m \Delta f \tau}, \dots, e^{-j2\pi(M-1)\Delta f \tau}]^T). \end{aligned} \quad (22)$$

the effective channel matrix of dimension  $N_{\text{rx}}^{\text{rf}} MN \times MN$ , defined for a single scatterer  $p$  is given by

$$\begin{aligned} \mathbf{G}_b(\tau_p, \nu_p, \theta_{p,j}, \phi_{k,p}) &\triangleq \\ &\mathbf{T} \otimes (\mathbf{U}_b^H \mathbf{b}(\theta_{p,j}, \gamma_{p,j}) \mathbf{a}^H(\phi_{k,p}, r_{k,p}) \mathbf{f}_l) \end{aligned} \quad (23)$$

The received signal  $\underline{\mathbf{y}}_b \in \mathbb{C}^{N_{\text{rx}}^{\text{rf}} MN \times 1}$  can then be written as

$$\underline{\mathbf{y}}_b = \sum_{p=1}^P \varepsilon_p \mathbf{G}_b(\tau_p, \nu_p, \theta_{p,j}, \phi_{k,p}) \underline{\mathbf{x}}_b + \mathbf{w}_b. \quad (24)$$

For the derivation of the ML target parameter estimation in Section IV, we consider a single Tx and Rx pair and drop their respective indices,  $(\cdot)_{k,j}$ , to avoid excessive notation clutter. Needless to say, the same formulation holds for other pairs.

### IV. PARAMETER ESTIMATION AND DETECTION

Since we assume no a priori knowledge of the target's initial position in regard to the near/far-field, we introduce a *two-stage* ML parameter estimation framework. In the initial stage, radial segments of the beam space are covered using FF beamforming, and the target parameters are estimated based on bi-static FF assumptions at the Rx units. This scheme leads to a twofold advantage; 1) As depicted in Fig. 1 covering the beam space with beamforming vectors reduces the latency resulting from codeword selection since the FF codebook is

parameterized only in angle, whereas the NF codebook is two-dimensional. 2) As will be shown in this section, the parameter search space of the FF model is significantly smaller than that of the NF model, thereby reducing the parameter estimation complexity.

For the second stage, based on the estimates obtained from the first stage, if the target is determined to be in the NF region of either the Tx or Rx units, a second estimation stage is performed. Depending on the target being located in the NF of the Tx or Rx, the second stage will differ, as will be outlined in the following.

Important to note that when the NF cases occur in the initial stage, the model mismatch between the NF and FF array steering vectors presented in Section II-C leads to poorly localized estimates. However, these approximate and inaccurate estimates are used to define a *region of interest* for further processing based on the correct (i.e. NF) model.

#### A. Maximum likelihood parameter estimation

Considering that the delay parameter can be written as  $\tau = (r + \gamma)/c$ , and therefore parameterizing  $\mathbf{T}(\tau, \nu) \rightarrow \mathbf{T}(r, \gamma, \nu)$ , we denote the true value of target parameters as  $\hat{\boldsymbol{\theta}} = \{\hat{\varepsilon}_p, \hat{\nu}_p, \hat{r}_p, \hat{\gamma}_p, \hat{\theta}_p, \hat{\phi}_p\}_{p=0}^{P-1}$ . For each  $b \in [B]$ , the effective channel matrix of dimension  $N_{\text{rf}}NM \times NM$  associated with scattering point  $p$  is given as  $\mathbf{G}_b(\hat{\nu}_p, \hat{r}_p, \hat{\gamma}_p, \hat{\theta}_p, \hat{\phi}_p)$  in (23). The received signal then takes the form

$$\underline{\mathbf{y}}_b = \sum_{p=0}^{P-1} \hat{\varepsilon}_p \mathbf{G}_b(\hat{\nu}_p, \hat{r}_p, \hat{\gamma}_p, \hat{\theta}_p, \hat{\phi}_p) \underline{\mathbf{x}}_b + \mathbf{w}_b. \quad (25)$$

Given knowledge of the number of scattering points  $P$ , the ML estimate of the set  $\hat{\boldsymbol{\theta}}$  can be obtained by solving (27), where the space is  $\Gamma \triangleq \mathbb{C}^P \times \mathbb{R}^{5P}$ .

Solving (27) requires knowledge of the number of scattering points  $P$ , which can be formulated as a model order estimation problem. Since the *micro-scatterers* of extended targets are often indistinguishable, the estimation of the model order is an unattainable task due to the problem being intrinsically ill-posed [26]. In addition, the parameter space of the brute force ML solution in (27) requires prohibitively large computations. Therefore, we resort to an approximate method that evaluates a hypothesis test on a set of  $(\nu_p, r_p, \gamma_p, \theta_p, \phi_p)$  tuples belonging to a grid  $\Theta$ . This approach involves a detection and estimation step for each parameter tuple. Specifically, we formulate the target detection as a standard Neyman-Pearson hypothesis testing problem [27], for which the solution that maximizes the detection probability subject to a bound on the false-alarm probability is given by the Likelihood Ratio Test with hypotheses  $\mathcal{H}_0$  and  $\mathcal{H}_1$  corresponding to the absence or presence of a target (see [5] for details). To formulate this problem, the log-likelihood ratio for the binary hypothesis

testing problem given by

$$\ell(\varepsilon, \nu, r, \gamma, \theta, \phi) = \log \frac{\exp\left(-\frac{1}{\sigma_w^2} \sum_{b=1}^B \|\underline{\mathbf{y}}_b - \varepsilon \mathbf{G}_b \underline{\mathbf{x}}_b\|_2^2\right)}{\exp\left(-\frac{1}{\sigma_w^2} \sum_{b=1}^B \|\underline{\mathbf{y}}_b\|_2^2\right)} \quad (28)$$

is compared against a threshold for every point in  $\Theta$ , resulting in the generalized likelihood ratio test

$$\ell(\nu, r, \gamma, \theta, \phi) \underset{\mathcal{H}_0}{\overset{\mathcal{H}_1}{\geq}} T_r, \quad (\nu, r, \gamma, \theta, \phi) \in \Theta \quad (29)$$

where the threshold  $T_r$  is chosen at each grid point by using the ordered statistic constant false alarm rate (OS-CFAR) technique described in [28]. For the binary hypothesis test above, the (generalized) log-likelihood ratio in (28) coincides with the likelihood function (52), derived in Appendix A and is given by

$$\ell(\nu, r, \gamma, \theta, \phi) = \frac{|\mathbf{f}^H \mathbf{a} \mathbf{b}^H \boldsymbol{\xi}_{(B)}(r, \gamma, \nu)|^2}{\mathbf{f}^H \mathbf{a} \mathbf{b}^H \bar{\mathbf{U}}_{(B)} \mathbf{b} \mathbf{a}^H \mathbf{f}}. \quad (30)$$

Note that the ML function in (52) is valid considering a single scattering point. When dealing with multi-target scenarios that are well-separated (w.r.t. system resolution limits), recovery of the numerous scatterers requires an successive interference cancellation (SIC) technique, where the contribution of the estimated point is removed from the signal, and the metric is re-evaluated in an iterative manner until some stopping criteria are met. In extended-target scenarios where the micro-scatterers are often very closely spaced, the mutual influence caused by the ‘‘sidelobes’’ of the likelihood function for adjacent micro-scatterers renders dependency on the hypothesis testing for adjacent points. Therefore SIC techniques can be ineffective. However, as it will be shown in Section VI, the simple grid-based estimation and thresholding (detection) approach proposed above leads to satisfactory performance. Since we assume that the target location within the NF or FF of the arrays is initially unknown, to tackle the large search space of the refined grids over  $\Theta$  to obtain highly accurate estimates, we propose the two-stage ML estimation method that follows.

*Remark 4.* The term target ‘‘detection’’ in this section differs from that implying the detection of a target such as a vehicle as a potential communication UE described in Section II which can be achieved via communication. In the grided ML search above, the detection corresponds to distinguishing the response from a point scatterer (or multiple point scatterers that violate the system resolution limits and therefore show as a point response) from noise in the radar image, produced from evaluating (30) over the set of tuples on the defined grid.

**Stage 1: Far-field beamforming and bi-static estimation:** In the first stage, we assume no knowledge of the target position. The appropriate FF beamforming codeword is selected at the Tx, and based on the assumption that the extended target is located in the FF of both the Tx and Rx units, the array



$$\boldsymbol{\theta}_{\text{ML}} = \underset{\{\varepsilon_p, \nu_p, r_p, \gamma_p, \theta_p, \phi_p\}_{p=0}^{P-1} \in \Gamma}{\arg \min} \left\| \sum_{b=0}^{B-1} \mathbf{y}_b - \sum_{p=0}^{P-1} \varepsilon_p \mathbf{G}_b(\nu_p, r_p, \gamma_p, \theta_p, \phi_p) \mathbf{x}_b \right\|_2^2, \quad (27)$$

manifolds at the Tx and Rx units in (23), which are only functions of angular parameters, i.e. ( $\mathbf{a}(\phi, r) \rightarrow \mathbf{a}(\phi)$  and  $\mathbf{b}(\theta, \gamma) \rightarrow \mathbf{b}(\theta)$ ) are considered for parameter estimation. Additionally, since the delay cannot be estimated from the array manifold in this model, it has to be estimated based on the observed total time of flight  $\tau = (r + \gamma)/c$  from the sub-carrier dimension of the OFDM frames, i.e. the phase observed on the  $m\Delta f\tau$  component of the exponent in (21). The bi-static Doppler projection seen by each of the Rx units, given in (34), can be estimated over the OFDM symbol dimension, i.e. the phase observed on the  $nT_0\nu$  component of the exponent in (21) [29]. As such, the effective channel matrix  $\mathbf{G}_b(\nu_p, r_p, \gamma_p, \theta_p, \phi_p)$  in (23) takes the form

$$\check{\mathbf{G}}_b(\nu_p, \tau_p, \theta_p) \triangleq \mathbf{T} \otimes \left( \mathbf{U}_b^H \mathbf{b}(\theta_p) \mathbf{a}^H(\phi_p) \mathbf{f}(\hat{\phi}_p) \right). \quad (31)$$

Note that, from the bi-static Rx's perspective, the channel response from Tx to the target is a constant which can be absorbed in the channel gain coefficient, i.e. :

$$g_p \triangleq \mathbf{a}^H(\phi_p) \mathbf{f}(\hat{\phi}_p), \quad h_p \triangleq g_p \varepsilon_p$$

and therefore,  $\check{\mathbf{G}}_b$  is not a function of the AoD,  $\phi$ . Then, defining the true value of parameters as  $\hat{\boldsymbol{\theta}} = \{\hat{h}_p, \hat{\nu}_p, \hat{\tau}_p, \hat{\theta}_p\}_{p=0}^{P-1}$  the received signal then takes the form

$$\underline{\mathbf{y}}_b = \sum_{p=0}^{P-1} \hat{h}_p \check{\mathbf{G}}_b(\hat{\nu}_p, \hat{\tau}_p, \hat{\theta}_p) \mathbf{x}_b + \mathbf{w}_b. \quad (32)$$

Where for an extended target with  $P$  scattering points, the ML estimate of the set  $\hat{\boldsymbol{\theta}}$  involves a search in a  $\Gamma_{\text{FF}} \triangleq \mathbb{C}^P \times \mathbb{R}^{3P}$  space. Similar to the derivation of the likelihood function in the previous section, the likelihood function of the FF model is obtained, which is omitted here for brevity. Note that in this case, the maximization of the log-likelihood function is performed with respect to  $h_p$  for fixed  $(\nu, \tau, \theta)$  to obtain:

$$\ell(\nu, \tau, \theta) = \frac{\left| \mathbf{b}^H \boldsymbol{\xi}_{(B)}(\tau, \nu) \right|^2}{\mathbf{b}^H \bar{\mathbf{U}}_{(B)} \mathbf{b}}, \quad (33)$$

By defining a suitably refined search grid on  $\Theta_{\text{FF}} \triangleq \mathbb{R}^{3P}$ , and evaluating (33) for every tuple  $(\nu, \tau, \theta) \in \Theta_{\text{FF}}$  and performing the estimation and detection (thresholding) step according to Section IV-A, the estimates  $(\hat{\nu}, \hat{\tau}, \hat{\theta})$  of the scattering points can be obtained. To convert these values to the angle and range of the target in the global coordinates, we use the bi-static conversion principles in the next section.

### B. Bi-static range and Doppler shift

In a bi-static configuration, the propagation time  $\tau_p$  of the signal scattered by a scatterer  $p$  is related to the distance

between the Tx and the scatterer,  $r_{\text{tx},p}$ , and that between the scatterer and the Rx,  $\gamma_{p,\text{rx}}$ , via the bi-static range,  $R_{\text{bis}} = r_{\text{tx},p} + \gamma_{p,\text{rx}} = \tau_p \cdot c$  [29]. After estimating  $R_{\text{bis}}$  via  $\tau_p$ , the scatterer can be located on an ellipse with a major axis equal to  $R_{\text{bis}}$  and foci at Tx and Rx positions, as depicted in the inset of Fig. 4. The Tx, Rx, and scatterer form a triangle with base  $\Delta$  (with  $\Delta$  the distance between Tx and Rx) called the baseline; the angle  $\beta$  of the opposite vertex is named the bi-static angle.

If the AoA  $\theta_{p,\text{rx}}$  of the reflected echo at the Rx can be estimated, it is possible to determine the distance  $r$  as [30]

$$\gamma_{p,\text{rx}} = \frac{R_{\text{bis}}^2 - \Delta^2}{2(R_{\text{bis}} + \Delta \sin(\theta_{p,\text{rx}} - \pi/2))} \quad (34)$$

and then the scatterer position

$$\mathbf{p}_p = (x_{\text{rx}} - \gamma_{p,\text{rx}} \cos \theta_{p,\text{rx}}, y_{\text{rx}} + \gamma_{p,\text{rx}} \sin \theta_{p,\text{rx}}). \quad (35)$$

In addition to the scatterer location, the bi-static velocity of the scatterer can be inferred from the bi-static Doppler shift. The latter is proportional to the rate of change of  $R_{\text{bis}}$ . When Tx and Rx are stationary, and the scatterer is moving with velocity  $\mathbf{v}_p$ , the Doppler shift can be obtained as [30]

$$\begin{aligned} \nu_p &= \nu_{\text{tx},p} + \nu_{p,\text{rx}} \\ &= \frac{1}{\lambda_c} \frac{d}{dt} [r_{\text{tx},p}(t) + \gamma_{p,\text{rx}}(t)] = \frac{2v_p}{\lambda_c} \cos \delta \cos(\beta/2) \end{aligned} \quad (36)$$

where  $\delta$  is the angle between the direction of the velocity and the bi-static bisector, and  $v_p = |\mathbf{v}_p|$ . While  $\beta$  can be easily determined by knowing  $\Delta$ ,  $r_{\text{tx},p}$ ,  $\gamma_{p,\text{rx}}$ , and  $\theta_{p,\text{rx}}$ , the angle  $\delta$  is unknown so only the bi-static velocity,  $v_{\text{bis}} = |\mathbf{v}_{\text{bis}}| = v_p \cos \delta$ , can be estimated by the system.

### Stage 2: Near-field estimation

The second stage is only carried out if the target is determined to be in the NF of the Tx or Rx units, based on the estimates obtained by evaluating the FF model in (33). Below we describe the second stage for each scenario.

**Near-field of Rx: Parameter estimation with reduced search space:** Assume the target is determined to lie in the NF of an Rx array. This means the ML metric in (30) needs to be evaluated on a fine-grained grid defined over  $\Theta$  to meet high accuracy localization requirements. It is clear that evaluating a 5-D search grid is computationally heavy. Therefore, we define a suitably refined Cartesian grid over the region of interest (RoI), indicated by the approximate estimates from the first stage. Subsequently, the coordinates of each cell in the grid are translated to the equivalent  $(r_p, \gamma_p, \theta_p, \phi_p)$  and the ML metric in (52) is evaluated.

*Discussion:* Note that the transition region between NF and FF does not have a hard cut-off, in the sense that FF beams already start to form after approximately  $D_{\text{ff}}/10$  [12], [11] with some phase variations. Therefore, as the radial distance from the array approaches this distance, the array manifold tends increasingly toward the FF model. This is important in that if a target is located in these transitional regions, it will not be critical to determine the NF or FF regime, and even the FF model will result in acceptable performance for parameter estimation. This effect is also evident from numerical results provided in Section VI-D, where the beamforming and beamfocusing schemes exhibit similar performance in these regions.

### Near-field of Tx: Beamfocusing and re-estimation

If the target is determined to be in the NF of an Tx array, this means that the illumination beamformer at the Tx cannot focus the beam in the intended location with full BF gain. In this case, a codeword from a custom-designed beamfocusing codebook is selected to focus the energy in the area estimated by the first stage. These codewords are designed (see Section V for details) to maintain a constant gain in an extended region (angle-range). This scheme provides a two-fold advantage. 1) Due to the increase in BF gain (and therefore higher SNR) after selecting the appropriate codeword, a re-estimation of the target parameters at the Rx leads to more accurate estimates. Note that in this case, the Rxs can use the FF model due to the deployment topology (see Fig. 4). 2) In the possible case that the target is also a communication user, the communication performance can be significantly increased. Since the beamfocusing illuminates an extended region with a constant gain if the true UE antenna location deviates slightly from the one estimated from the back-reflected signal, a good SNR can still be maintained. We further remark that, if the region of interest for the second stage is larger than the area covered by the NF codeword, multiple neighboring codewords can be used in time-division manner to cover the RoI for re-estimation.

## V. DESIGN OF THE BEAMFOCUSING WEIGHTS

### A. Related works

With increasing carrier frequencies of wireless communication networks and the deployment of large arrays, the NF region is significantly expanded. Thus FF-based beamforming techniques such as DFT codebooks can result in significant SNR losses, affecting both the communication and sensing performance of the system. More recently, there have been numerous works dealing with NF beamfocusing schemes, especially in the Reconfigurable Reflecting Surfaces domain, due to the large array sizes used therein [31], [32]. While a few works have investigated using beamfocusing weights obtained by conjugating the NF array response, others have resorted to optimization-based methods to obtain suitable weights [33], [9]. The most significant drawback of those methods is that a very accurate estimate of the intended user coordinates (equivalently *range* and *angle*) is required (see (7) for the array response). Even when ignoring the cost of obtaining such

---

### Algorithm 1 Algorithm for designing beamfocusing vectors

---

**for** codeword  $g \in \mathcal{C}_f$  **do**

- 1) choose solution tolerance  $\rho$ , Tikhonov regularizer  $\epsilon_T$ , set  $\mathbf{c}_g = e^{j*0G}$
- 2) initialize  $\mathbf{f}_g$   $\triangleright$  see **Initialization**
- 3) set  $\mathbf{c}_g$  to  $\mathbf{c}_g = e^{j\angle(\mathbf{A}^H \mathbf{f}_g)}$
- 4) fix  $\mathbf{c}_g$ , update new  $\mathbf{f}_g$  by obtaining the residual error from evaluating the unconstrained linear least-squares problem,  $\|\mathbf{b}_g - |\mathbf{A}^H \mathbf{f}_g|\|_2$ .
- 5) repeat steps (2 - 4) until the decrease in objective function has diminished to within  $\rho$ .

**end for**

#### Initialization

$$\begin{aligned} \mathbf{y}' &\leftarrow \mathbf{y}_g \odot \mathbf{c}_g && \triangleright \mathbf{y}_g \text{ is the mask corresponding to } \mathbf{f}_g \\ \mathbf{f}_g &\leftarrow (\mathbf{A}\mathbf{A}^H + \epsilon_T \mathbf{I}_{N_a})^{-1} \mathbf{A} \mathbf{y}' \end{aligned}$$


---

estimates, these techniques pose another significant challenge since the goal is to focus beams on the UE's antenna. In the very likely scenario of physically extended targets (e.g. motorbikes, bicycles, cars, etc.) the UE antenna can be located anywhere on the object and the estimated reflection points do not necessarily correspond to the reflections from the antenna. In other works NF codebook-based techniques have been employed. Some of the more promising approaches are the *Ring-type Codebook* designs [32], where a first layer phase distribution is calculated based on the Fresnel principle and is then superimposed with the codeword selected of a (FF) DFT codebook in the second layer. As shown in [32], such design lead to significant spectral leakages in unwanted locations which beats the purpose of user-interference reduction via beamfocusing. From the sensing perspective, this leads to reflection from unintended objects that may be located in the undesired illuminated areas. Considering the issues mentioned above, we devise a codebook-based scheme inspired by flat-top beamforming techniques that provide an (almost-) constant gain over an extended angular span (see [5] and references therein for details). In the case of beamfocusing for the NF, we present a method that aims to synthesize beamfocusing weights for array operation in NF such that an extended area is illuminated with a relatively constant gain.

As a last note, it should be pointed out that one could essentially view NF beamfocusing optimization problem as a 2-dimensional filter design problem. These problems have previously extensively been studied in [34], [35]. A very similar approach is the design of 2-D spatial filters in the form of azimuth-elevation response (i.e. radiation pattern) of antenna arrays (see e.g. [36]).

### B. Problem formulation

Let  $\mathbf{f}$  be a beamfocusing vector of dimension  $N_a$ . The complex-valued (amplitude and phase) beam pattern radiated by the array at each sampling tuple  $(\tilde{\phi}_i, \tilde{r}_j)$ ,  $i \in [G_\theta]$ ,  $j \in [G_r]$  of a discrete angular set  $\{\tilde{\Omega}\}$ , ( $|\tilde{\Omega}| = G_\theta$ ) and range set  $\{\tilde{\Gamma}\}$ , ( $|\tilde{\Gamma}| = G_r$ ) can be calculated as the inner product of

the vector  $\mathbf{f}$  and the array response vector  $\mathbf{a}(\phi, r)$  at the given grid angle-range tuple i.e.,  $\mathbf{a}^H(\tilde{\phi}_i, \tilde{r}_j)\mathbf{f}$ .

The design problem of interest is to find  $\mathbf{f}$  to approach a desired radiation pattern  $\bar{\mathbf{b}} \in \mathbb{R}_+^G$ . The entries of  $\bar{\mathbf{b}} = [\bar{b}_1, \dots, \bar{b}_G]$  are magnitudes of the radiation pattern at each of the  $G = G_\theta G_r$  discrete tuple points. In particular, we fix  $\bar{\mathbf{b}}$  to have a constant level in a pre-determined angle-range zone (i.e. spot) in the NF of the array and such that the values corresponding to the rejection directions (sidelobes) are below a certain threshold with respect to the maximum (center beam). By letting  $\mathbf{A} = [\mathbf{a}(\tilde{\phi}_1, \tilde{r}_1), \dots, \mathbf{a}(\tilde{\phi}_{G_\theta}, \tilde{r}_{G_r})] \in \mathbb{R}^{N_a \times G}$ , this problem can be formulated as a magnitude least-squares problem which belongs to the class of problems addressed by [37], [38].

$$\begin{aligned} \min_{\mathbf{f}} \quad & \|\mathbf{A}^H \mathbf{f} - \bar{\mathbf{b}}\|_2^2 \\ \text{s.t.} \quad & \mathbf{f}^H \mathbf{A} \mathbf{A}^H \mathbf{f} = 1 \end{aligned} \quad (37)$$

where the constraint in (37) imposes unit transmit power. Depending on the operating scenario, a beam pattern can focus the transmitted energy on a certain given angle-range sector (i.e., field of view (FoV) equal to  $\Omega \times \Gamma$ ). In order to define our design in a flexible manner, the FoV is divided into multiple sectors as depicted in Fig. 1b, each sector determining the illumination area of a codeword (i.e. the span of the beamfocusing *spots*). These codewords are gathered in a codebook  $\mathcal{C}_f$ . Note that the problem in (37) aims to approximate the phase and magnitude of the reference mask, which gives a more constrained, but less localized solution, as required by our particular application. To relax this, we consider only the magnitude response in the optimization problem:

$$\begin{aligned} \min_{\mathbf{f}} \quad & \|\mathbf{A}^H \mathbf{f} - \bar{\mathbf{b}}\|_2^2 \\ \text{s.t.} \quad & \mathbf{f}^H \mathbf{A} \mathbf{A}^H \mathbf{f} = 1 \end{aligned} \quad (38)$$

The above problem is not convex, and therefore by performing a semidefinite relaxation, acceptable solutions can be obtained. Important to note that, in the case of one-dimensional filters and uniformly spaced linear arrays, one-dimensional spectral factorizations of magnitude responses are guaranteed to exist, and therefore the problem is significantly less complex than a multidimensional case, such as in this problem [38]. By defining  $\mathbf{B} = \text{diag}(\bar{\mathbf{b}})$  and restructuring the objective in (38) as:

$$\begin{aligned} \min_{\mathbf{f}, \mathbf{c}} \quad & \|\mathbf{A}^H \mathbf{f} - \mathbf{B} \mathbf{c}\|_2^2 \\ \text{s.t.} \quad & |\mathbf{c}| = \mathbf{1} \end{aligned} \quad (39)$$

It is possible to minimize firstly over  $\mathbf{f}$  and then minimize over  $\mathbf{c}$ , leading to:

$$\min_{|\mathbf{c}|=1} (\min_{\mathbf{f}} \|\mathbf{A}^H \mathbf{f} - \mathbf{B} \mathbf{c}\|_2^2) \quad (40)$$

Where, with the assumption that  $\mathbf{A}$  has full rank, the inner minimization problem has an analytic solution w.r.t.  $\mathbf{c}$ , i.e.

$(\mathbf{A} \mathbf{A}^H)^{-1} \mathbf{A} \mathbf{B} \mathbf{c}$ . Define  $\mathbf{W} = \mathbf{A}^H (\mathbf{A} \mathbf{A}^H)^{-1} \mathbf{A} \mathbf{B} - \mathbf{B}$ , then the problem can be formulated as below:

$$\begin{aligned} \min_{\mathbf{c}} \quad & \mathbf{c}^H \mathbf{W}^H \mathbf{W} \mathbf{c} \\ \text{s.t.} \quad & |\mathbf{c}| = \mathbf{1} \end{aligned} \quad (41)$$

Note that, due to the fine-grained grid which is used for the sampling points (i.e.  $G_r, G_\theta$ ) of the array manifold matrix  $\mathbf{A}$ , this matrix is often not full rank (i.e.  $\text{rank}(\mathbf{A}) < \#\text{cols}(\mathbf{A})$ ), and therefore the solution in (40) does not hold. To overcome this one can use a *Tikhonov* regularization with parameter  $\epsilon_T \in \mathbb{R}_+$  and re-formulate the problem as:

$$\min_{\mathbf{f}, \mathbf{c}} \|\mathbf{A}^H \mathbf{f} - \mathbf{B} \mathbf{c}\|_2^2 + \epsilon_T \|\mathbf{f}\|_2^2 \quad (42)$$

Then, equivalently by defining  $\mathbf{U} = \mathbf{A}^H (\mathbf{A} \mathbf{A}^H + \epsilon_T \mathbf{I}_{N_a})^{-1} \mathbf{A} - \mathbf{I}$  and  $\mathbf{W} = (\mathbf{U} \mathbf{B})^H (\mathbf{U} \mathbf{B})$  and

$$\tilde{\mathbf{W}} = \begin{bmatrix} \text{Re}(\mathbf{W}) & -\text{Im}(\mathbf{W}) \\ \text{Im}(\mathbf{W}) & \text{Re}(\mathbf{W}) \end{bmatrix} \quad (43)$$

and defining  $\mathbf{V} = \epsilon_T ((\mathbf{A} \mathbf{A}^H + \epsilon_T \mathbf{I}_{N_a})^{-1} \mathbf{A} \mathbf{B})^H (\mathbf{A} \mathbf{A}^H + \epsilon_T \mathbf{I}_{N_a})^{-1} \mathbf{A} \mathbf{B}$ , and  $\tilde{\mathbf{V}}$  in similar fashion as  $\tilde{\mathbf{W}}$ , the following problem should be solved:

$$\begin{aligned} \min_{\mathbf{C}} \quad & \text{trace}(\mathbf{C} \tilde{\mathbf{W}}) + \text{trace}(\mathbf{C} \tilde{\mathbf{V}}) \\ \text{s.t.} \quad & \mathbf{C}_{ii} + \mathbf{C}_{jj} = 1 \\ & \mathbf{C} \succeq 0 \end{aligned} \quad (44)$$

Then, the beamforming vector can be found as  $\mathbf{f} = (\mathbf{A} \mathbf{A}^H + \epsilon_T \mathbf{I}_{N_a})^{-1} \mathbf{A} \mathbf{B} \mathbf{c}$ . Above,  $\mathbf{C} \in \mathbb{R}^{2G \times 2G}$  is diagonalized from the real and imaginary part of  $\mathbf{c}$  as  $\mathbf{C} = \text{diag}(\mathbf{c}_r \mathbf{c}_r^T, \mathbf{c}_i \mathbf{c}_i^T)$ .

Given the typically large number of columns in  $\mathbf{A} \in \mathbb{R}^{N_a \times G}$ , the program in (44), which involves matrix inversion in the step obtaining  $\mathbf{U}$  is memory and computationally exhaustive (this is especially true when using CVX solvers). Therefore we solve the beam design problem in (39) using an iterative method. This method is based on the fact that for fixed  $\mathbf{c}$ ,  $\mathbf{f}$  can be found as the solution to a linear least-squares problem. Then, for fixed  $\mathbf{f}$  the optimal  $\mathbf{c}$  is equal to a complex number with modulus 1, with its phase equal to  $\angle(\mathbf{A}^H \mathbf{f})$ . The details of this procedure are provided in Algorithm 1. Two examples of the obtained beamfocusing radiation patterns and the corresponding masks are shown in Fig. 5.

*Remark 5.* The masks  $\bar{\mathbf{b}} \in \mathbb{R}^G$  as defined above, consist of sharp transitions from the desired spot to the region outside the spot. For a filter design problem, these transitions can lead to instabilities. Moreover, due to the nonlinearity of wave propagation principles, beamfocusing vectors for masks that are wide and long (i.e. large span in angle and range) are difficult to synthesize (compare for example Fig. 5 and Fig. 6). This is especially true when steering toward the non-boresight directions. In order to mitigate this issue we propose the use of *windowing* functions on the mask to create a smooth transition and concentrate the energy in a more centralized manner. An example of this can be seen in Fig. 6 using a 2-D Kaiser window.

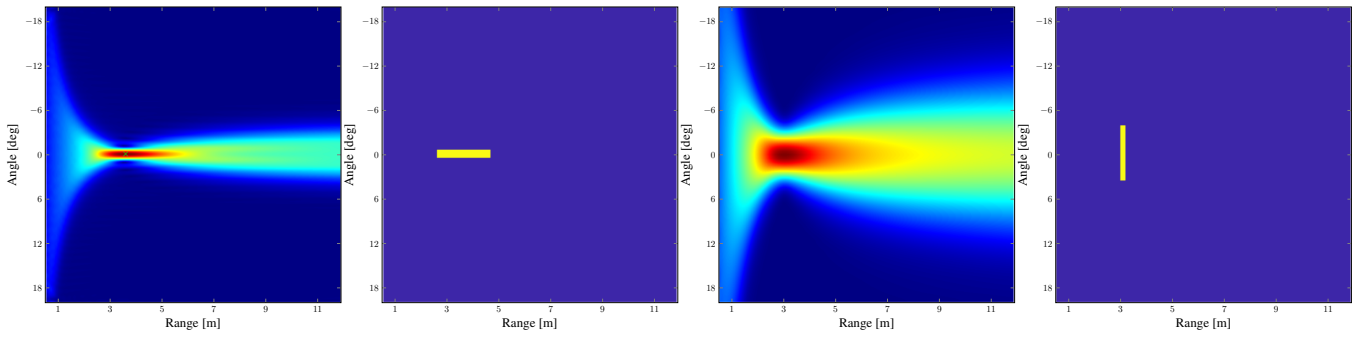


Fig. 5: Examples of beamfocusing codewords and corresponding masks. Note that the masks are defined either to concentrate the radiated energy over extended distances (left) or an extended angular span (right).

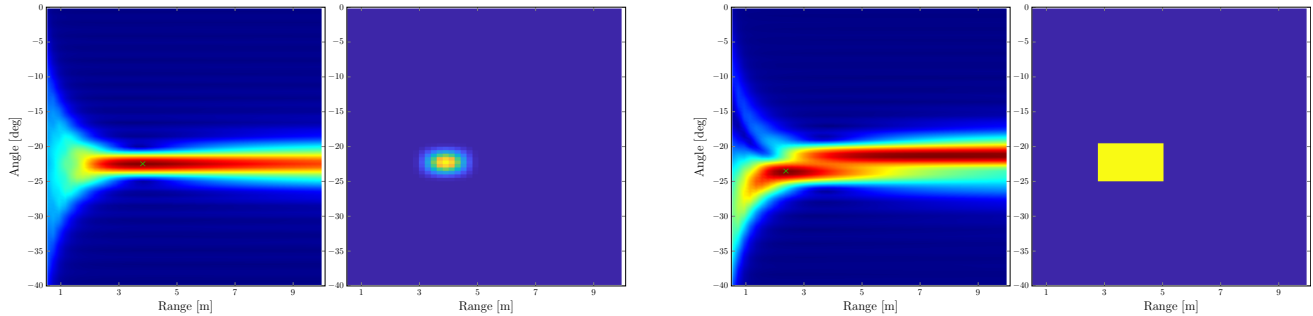


Fig. 6: Example of beamfocusing codewords derived for (a) Smoothed mask with a Kaiser window with a shape factor of 5.5, (b) without mask smoothing. Note that in this case, the mask spans a relatively wide angular/distance section as compared to the mask in Fig. 5.

## VI. SIMULATION RESULTS

In this section, we present numerical results to evaluate the effectiveness of the proposed schemes. The results in this section are based on the scenario and topology in Fig. 4, where we consider numerous trajectories, enumerated I-IV, to simulate the different conditions that may be encountered in a real-world deployment. Unless otherwise stated, at each location along the trajectories, we consider an instance of the extended target generated according to the BND in Section II-A and with the dimensions provided Tab. I. Note that the grids defined for parameter estimation do not coincide with the grid used in Section II-A and Tab. II to simulate the BND extended target.

### A. Far-field estimation performance (Trajectory I)

Referring to Fig. 4, the extended target moving along Trajectory I is located entirely in the FF of the Tx and both Rx arrays. Figure 7 shows the estimated spatial parameters of the extended target. At each step, the extended target is generated 100 times in Monte-carlo (MC) fashion, independently for each of the Rx units. The boxes indicate all the point estimates that pass the OS-CFAR threshold and have an amplitude within 3dB of the main peak, local to each Rx. These bounding boxes are obtained as the minimum box that fits the convex hull contacting the above-mentioned detection points. Since the main peak from the ML metric in the angle/range domain is wide and leaks into the neighboring bins, the points lying on this main peak also pass the CFAR and lead to enlarged boxes.

The system parameters considered in the simulations lead to a bi-static range resolution of approx. 2.34 [m] and angular resolution of approx.  $2.2^\circ$ , which are clearly inadequate to resolve the individual scatters in the simulated target box in most cases. Therefore one can calculate a weighted estimate of the detected points after thresholding where the weight of each estimated point corresponds to the value from evaluating (33). Then the weighted average estimate of the target is obtained and plotted in Fig. 7 as the crosses and circles. From this, it can be observed that the estimated target location is very accurate. Note that up to an extent, super-resolution techniques (e.g. sub-space-based methods) can be used alternatively, however, this is out of scope for this paper. To further demonstrate the accuracy of the FF estimation, we calculate the root mean square error (RMSE) between the **main** peak at each iteration of the MC process and the center of the box (target). This is plotted in Fig. 7(b).

### B. Multi-static spatial diversity gain (Trajectory IV)

In this setup, we aim to demonstrate the effectiveness of multi-static configurations. More specifically, it is well known that under different aspect angles under which targets are observed by the Rx units in multi-static configurations, targets can exhibit very different reflection characteristics [39]. To this end, having multiple Rx's increases robustness in terms of detection. Given that an important distinction of radar systems utilizing multiple radars is to incorporate some level of data fusion between the measurement of individual sensors, we



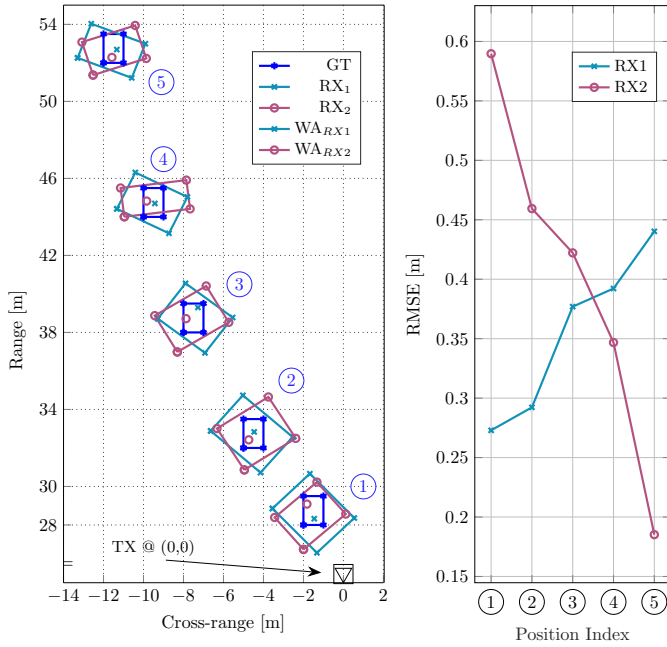


Fig. 7: Far-field estimates of the extended target along trajectory I in Fig. 4.

perform the following experiment to demonstrate this. Figure 8 depicts the average detection probability of the considered extended target at each Rx, simulated 200 times for each Rx at the given points along Trajectory IV in Fig. 4, where the detection is performed locally at each Rx using the OS-CFAR thresholding technique. A detection is declared if the main peak passes the threshold and the estimated position resulting from the peak value satisfies  $\sqrt{(\hat{x}_p - x_p)^2 + (\hat{y}_p - y_p)^2} < 1$  [m]. Important to note that, each realization is performed according to the BND. This means that in some instances a Rx may observe very few or even zero scattering points from the extended target. The *Fused* curve, shows the average detection probability if at each step, either one of the Rxs has detected the target (i.e. OR operation). This fusion can be performed at a central node.

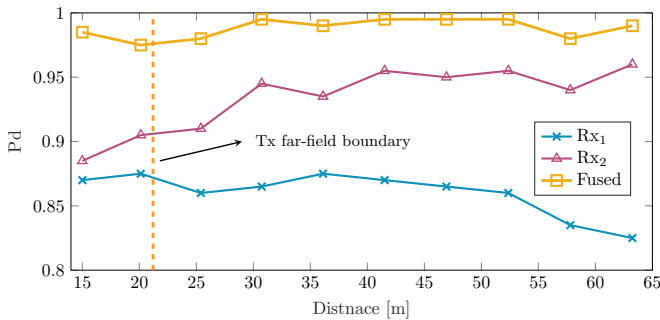


Fig. 8: Probability of detection for an extended target along trajectory IV in Fig. 4. The x-axis indicates radial distance from the Tx.

### C. Estimation of targets in receiver NF (Trajectory III)

In Fig. 4, the extended target moving along Trajectory III is initially estimated to lie in the NF of Rx<sub>1</sub>. Figure 9 shows the estimates obtained from using the FF mismatched model (evaluating (33)) at the first stage. Then by defining an RoI based on these estimates, we evaluate (52) on a fine-grained grid defined over the RoI, comprising a  $6 \times 6$  [m<sup>2</sup>] square with 0.05 [m] pixels. Figure 9a corresponds to the closer target location on the trajectory, where it can be observed that it is possible to individually resolve many of the point scatterers with high accuracy (much superior to the bandwidth imposed range resolution). Figure 9b depicts the same procedure, however since the target is now further from Rx<sub>1</sub>, the individual scattering points can not be resolved. Nonetheless, the estimated location is highly accurate. Note that the estimates obtained by Rx<sub>2</sub> for both positions correspond to the FF model and since the target lies in its FF, the estimates are accurate within the system limits (i.e. range and angular resolution).

### D. Spectral efficiency enhancement with beamfocusing (Trajectory II)

By considering a LoS channel with free-space path loss  $PL = (4\pi r/\lambda)^2$ , the matching gain  $G_M$  and achievable spectral efficiency are respectively given by

$$G_M = |\mathbf{a}^H(r_0, \phi_0) \mathbf{f}_X(\hat{r}, \hat{\phi})| \quad (45a)$$

$$SE = \log_2 \left( 1 + \frac{P_{tx} |G_M|^2}{N_0 W} \left( \frac{\lambda}{4\pi r_0} \right)^2 \right), \quad (45b)$$

with  $(r_0, \phi_0)$  being the true location of the target, and the parameter values specified in Tab. I.  $\mathbf{f}_X \in \{\mathbf{f}_N, \mathbf{f}_F\}$  is the Tx beamforming (/beamfocusing) vector where  $\mathbf{f}_F(\hat{\phi})$  is a codeword chosen from a discrete *Fourier* codebook  $\in \mathbb{C}^{N_a \times N_a}$ , as the codeword with the closest angular distance of the mainlobe peak with respect to the estimated AoD  $\hat{\phi}$ .

$\mathbf{f}_N(\hat{r}, \hat{\phi})$  is a codeword from the *custom-designed* codebook of beamfocusing vectors, as explained in Section V. Figures 10, 11, show the matching gain and achievable spectral efficiency (SE) for the extended target along Trajectory II, respectively. The plots are obtained by calculating the matching gain and SE at a hypothetical user antenna that is mounted on the extended target. Since the custom beamfocusing vectors are designed to cover an extended area with a constant gain as in Fig. 1b, if the antenna position deviates from the expected location, the Fourier codeword performs significantly worse than beamfocusing words. To demonstrate the parameter estimation performance with beamfocusing and beamforming more explicitly, we consider a single-point scatterer at each of the locations along Trajectory II and perform parameter estimation (at Rx) using beamformed and beam-focused transmission. The results in Fig. 12 indicate an improved parameter estimation which can be attributed to the increase in SNR at the target location.

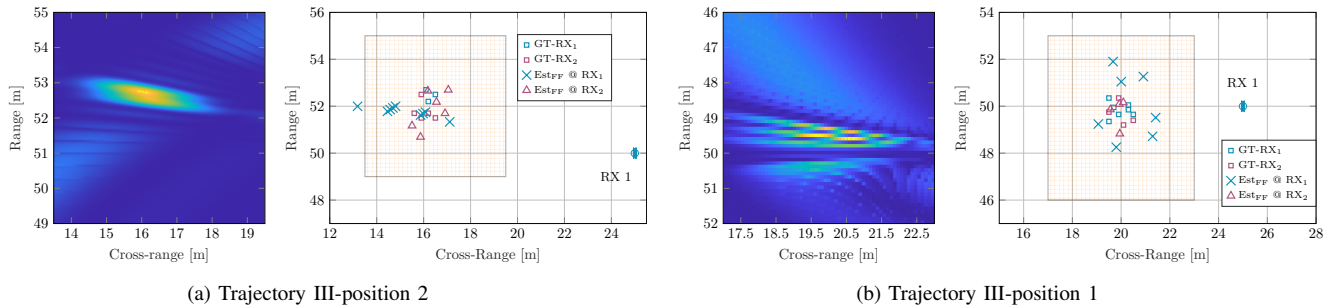


Fig. 9: The figure shows an extended target located in the NF of  $RX_1$  (Trajectory III of Fig. 4). After performing an ML estimation based on FF-bi-static assumptions, the estimated scattering points from  $RX_1$  indicate the target to be in the NF of this RX unit. Then, a fine-grained search grid is defined in the indicated RoI, where the ML metric in (52) is evaluated as shown on the left for each target.

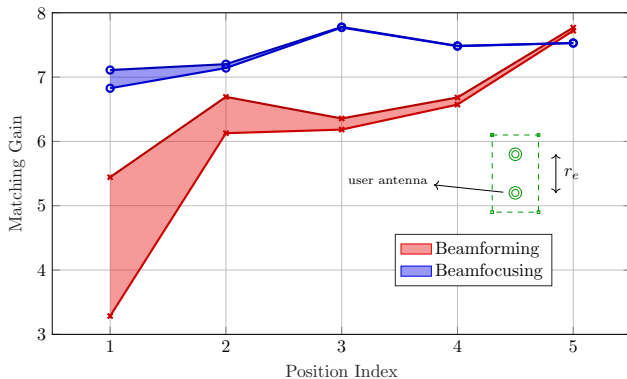


Fig. 10: Matching gain from beamfocusing and beamforming an extended target along trajectory II in Fig. 4, where the target locations are indexed 1–5. The filled area shows the gain within a mismatched antenna distance  $r_e = 1$  [m] on the extended object.

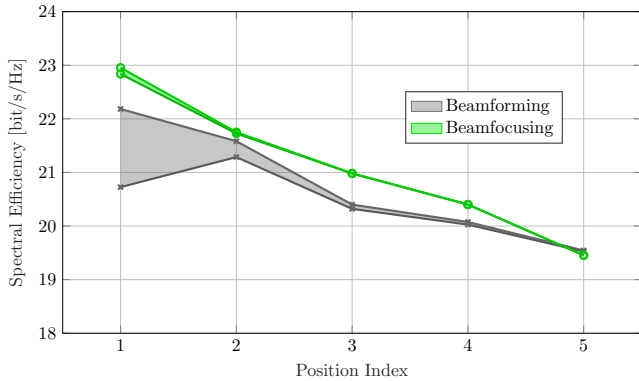


Fig. 11: Spectral efficiency from beamfocusing and beamforming an extended target along trajectory II in Fig. 4, where the target locations are indexed 1–5. The filled area shows the gain within a mismatched antenna distance  $r_e = 1$  [m] on the extended object.

## VII. CONCLUSION

In this work, we propose a two-stage parameter estimation framework for ISAC in a multi-static configuration. The framework performs beamforming and ML parameter estimation based on the FF assumption in the first stage. The second stage of the scheme is deployed when the estimation results

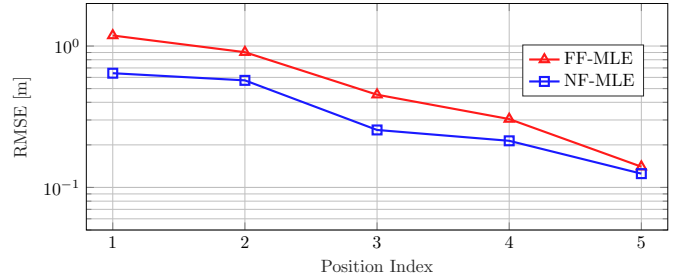


Fig. 12: Comparison of the estimation error of the target position using a NF codeword and FF codeword.

TABLE I: System parameters

$N = 100$	$M = 6$
$f_c = 28.0$ [GHz]	$W = 128$ [MHz]
$P_{avg} = 26$ [dBm]	$\sigma_{rcs} = 1$ [m <sup>2</sup> ], $P_{fa} = 10^{-3}$
Noise Figure (NF) = 3 [dB]	Noise PSD = $2 \cdot 10^{-21}$ [W/Hz]
$N_a = 64$	$N_{rf} = 8, B = 1$

of the first stage indicate the sensing target to be located in the NF of the arrays. In particular, if the target is located in the NF of the Rx arrays, a high-dimensional ML parameter estimation based on the exact signal model (i.e. exact array response model) is carried out in a defined region of interest. If the target is determined to be in the NF of the Tx array, the scheme selects beamfocusing codewords, which are designed via solving a magnitude least squares problem, to illuminate the target and the Rxs re-estimate the target parameters.

## ACKNOWLEDGMENT

The authors would like to acknowledge the financial support by the Federal Ministry of Education and Research of Germany in the program of “Souverän. Digital. Vernetzt.” Joint project 6G-RIC, project identification number: 16KISK030, and by the European Union under the Italian National Recovery and Resilience Plan (NRRP) of NextGenerationEU, part-

TABLE II: Target parameters (see Fig.2)

Max. length $T_l = 1.5$ [m]	Max. width $T_w = 1$ [m]
BNM parameter $q \approx 0.01$	Grid size $T_g = 0.1$ [m]

nship on “Telecommunications of the Future” (PE00000001 - program “RESTART”).

#### APPENDIX A DERIVATION OF ML ESTIMATE

Here we derive the ML estimate for a single scattering point  $p$ . For ease of notation, we drop some of the arguments. The likelihood-function of  $\underline{\mathbf{y}}_b$  in (24) is :

$$L(\underline{\mathbf{y}}_b; (\varepsilon_p, \nu_p, r_p, \gamma_p, \theta_p, \phi_p)) = \frac{1}{\det(2\pi\sigma^2 \mathbf{I}_{NMN_{rf}})^{1/2}} \exp\left(-\frac{1}{2\sigma^2} \left( (\underline{\mathbf{y}}_b - \varepsilon \mathbf{G}_b \underline{\mathbf{x}}_b)^H (\underline{\mathbf{y}}_b - \varepsilon \mathbf{G}_b \underline{\mathbf{x}}_b) \right)\right). \quad (46)$$

Accumulating all observations up to the  $B$ -th slot,  $\underline{\mathbf{y}}^{(B)} = [\underline{\mathbf{y}}_1, \dots, \underline{\mathbf{y}}_B]$ , the log-likelihood function is given by:

$$\begin{aligned} \ell(\underline{\mathbf{y}}^{(B)}; (\varepsilon_p, \nu_p, r_p, \gamma_p, \theta_p, \phi_p)) &= \log\left(\underline{\mathbf{y}}^{(B)}; (\varepsilon_p, \nu_p, r_p, \gamma_p, \theta_p, \phi_p)\right) \\ &= \sum_{b=1}^B \log\left(L(\underline{\mathbf{y}}_b; (\varepsilon_p, \nu_p, r_p, \gamma_p, \theta_p, \phi_p))\right). \end{aligned} \quad (47)$$

Using the ML estimation procedure for unknown parameters described in [40] and using (47), the ML estimate in the  $b$ -th block is given

$$\begin{aligned} (\hat{\varepsilon}_p, \hat{\nu}_p, \hat{r}_p, \hat{\gamma}_p, \hat{\theta}_p, \hat{\phi}_p) &= \underset{\varepsilon_p, \nu, r, \gamma, \theta, \phi}{\operatorname{argmax}} \ell(\underline{\mathbf{y}}^{(B)}; (\varepsilon_p, \nu_p, r_p, \gamma_p, \theta_p, \phi_p)) \\ &= \underset{\varepsilon_p, \nu, r, \gamma, \theta, \phi}{\operatorname{argmin}} \sum_{b=1}^B \left\| \underline{\mathbf{y}}_b - \varepsilon_p \mathbf{G}_b(\nu_p, r_p, \gamma_p, \theta_p, \phi_p) \underline{\mathbf{x}}_b \right\|_2^2 \\ &= \underset{\varepsilon_p, \nu, r, \gamma, \theta, \phi}{\operatorname{argmin}} \sum_{b=1}^B \left\{ |\varepsilon_p|^2 \underline{\mathbf{x}}_b^H \mathbf{G}_b^H \mathbf{G}_b \underline{\mathbf{x}}_b - 2\operatorname{Re} \left\{ (\varepsilon_p)^* \underline{\mathbf{x}}_b^H \mathbf{G}_b^H \underline{\mathbf{y}}_b \right\} \right\}. \end{aligned} \quad (48)$$

defining:

$$\begin{aligned} \bar{\mathbf{U}}_{(B)} &= \sum_{b=1}^B \|\underline{\mathbf{x}}_b\|_2^2 \mathbf{U}_b \mathbf{U}_b^H \\ \xi_{(B)}(r, \gamma, \nu) &= \left[ \sum_{b=1}^B \underline{\mathbf{x}}_b^T \mathbf{T}(r, \gamma, \nu) \mathbf{Y}_b^H \mathbf{U}_b^H \right], \end{aligned}$$

Denoting  $\mathbf{Y}_b = [\mathbf{y}_b[0, 0], \dots, \mathbf{y}_b[N-1, M-1]] \in \mathbb{C}^{N_a \times NM}$ , and using

$$\begin{aligned} \mathbf{G}_b^H \mathbf{G}_b &= (\mathbf{T} \otimes \mathbf{U}_b^H \mathbf{b} \mathbf{a}^H \mathbf{f})^H (\mathbf{T} \otimes \mathbf{U}_b^H \mathbf{b} \mathbf{a}^H \mathbf{f}) \\ &\stackrel{(a)}{=} (\mathbf{T}^H \mathbf{T} \otimes \mathbf{f}^H \mathbf{a} \mathbf{b}^H \mathbf{U}_b \mathbf{U}_b^H \mathbf{b} \mathbf{a}^H \mathbf{f}) \\ &= \mathbf{f}^H \mathbf{a} \mathbf{b}^H \mathbf{U}_b \mathbf{U}_b^H \mathbf{b} \mathbf{a}^H \mathbf{f} \mathbf{I}_{NM} \end{aligned} \quad (49)$$

and

$$\begin{aligned} \mathbf{G}_b^H \mathbf{y}_b &= (\mathbf{T} \otimes \mathbf{U}_b^H \mathbf{b} \mathbf{a}^H \mathbf{f})^H \mathbf{y}_b \\ &= (\mathbf{T}^H \otimes \mathbf{f}^H \mathbf{a} \mathbf{b}^H \mathbf{U}_b) \mathbf{y}_b \\ &\stackrel{(b)}{=} \operatorname{vec}(\mathbf{f}^H \mathbf{a} \mathbf{b}^H \mathbf{U}_b \operatorname{vec}^{-1}(\mathbf{y}_b) \mathbf{T}^H) \\ &\stackrel{(c)}{=} (\mathbf{f}^H \mathbf{a} \mathbf{b}^H \mathbf{U}_b \mathbf{Y}_b \mathbf{T}^H)^T \\ &= \mathbf{T}^H \mathbf{Y}_b^T \mathbf{U}_b^T \mathbf{b}^* \mathbf{a}^T \mathbf{f}^*, \end{aligned} \quad (50)$$

where (a) stems from mixed property of the Kronecker product:  $(\mathbf{A} \otimes \mathbf{B})(\mathbf{C} \otimes \mathbf{D}) = (\mathbf{A}\mathbf{C} \otimes \mathbf{B}\mathbf{D})$ , (b) from the mixed Kronecker matrix-vector product:  $(\mathbf{A} \otimes \mathbf{B})\mathbf{v} = (\mathbf{B}\mathbf{V}\mathbf{A}^T)$ , where  $\mathbf{V} = \operatorname{vec}^{-1}(\mathbf{v})$ , and (c)  $\operatorname{vec}(\cdot)$ -operator applied to row-vector is equivalent to transposing.

For a given  $(\nu_p, r_p, \gamma_p, \theta_p, \phi_p)$  tuple, the value  $\varepsilon'$  which maximizes (48) is the maximum likelihood estimate of the channel coefficient given that a scattering point is present at  $(\nu_p, r_p, \gamma_p, \theta_p, \phi_p)$ , which can be evaluated in close form and is given by

$$\varepsilon'_p = \frac{\mathbf{f}^H \mathbf{a} \mathbf{b}^H \xi_{(B)}(r, \gamma, \nu)}{\mathbf{f}^H \mathbf{a} \mathbf{b}^H \bar{\mathbf{U}}_{(B)} \mathbf{b} \mathbf{a}^H \mathbf{f}}, \quad (51)$$

Substituting expression (51) into Eq. (48), the ML estimate can then be derived as:

$$(\hat{\nu}_p, \hat{r}_p, \hat{\gamma}_p, \hat{\theta}_p, \hat{\phi}_p) = \underset{\nu, r, \gamma, \theta, \phi}{\operatorname{argmax}} \frac{\left| \mathbf{f}^H \mathbf{a} \mathbf{b}^H \xi_{(B)}(r, \gamma, \nu) \right|^2}{\mathbf{f}^H \mathbf{a} \mathbf{b}^H \bar{\mathbf{U}}_{(B)} \mathbf{b} \mathbf{a}^H \mathbf{f}}, \quad (52)$$

where the space is  $\Gamma_{\text{ML}} \triangleq \mathbb{R}^{5P}$ .

#### REFERENCES

- [1] D. K. P. Tan, J. He, Y. Li, A. Bayesteh, Y. Chen, P. Zhu, and W. Tong, “Integrated sensing and communication in 6G: Motivations, use cases, requirements, challenges and future directions,” in *2021 1st IEEE International Online Symposium on Joint Communications & Sensing (JC&S)*. IEEE, 2021, pp. 1–6.
- [2] F. Liu, Y. Cui, C. Masouros, J. Xu, T. X. Han, Y. C. Eldar, and S. Buzzi, “Integrated sensing and communications: Toward dual-functional wireless networks for 6g and beyond,” *IEEE journal on selected areas in communications*, vol. 40, no. 6, pp. 1728–1767, 2022.
- [3] M. Braun, C. Sturm, and F. K. Jondral, “Maximum likelihood speed and distance estimation for OFDM radar,” in *Proc. IEEE Radar Conf.*, Arlington, VA, USA, May 2010, pp. 256–261.
- [4] C. B. Barneto, T. Riihonen, M. Turunen, L. Anttila, M. Fleischer, K. Stadius, J. Ryyänen, and M. Valkama, “Full-duplex OFDM radar with LTE and 5G NR waveforms: challenges, solutions, and measurements,” *IEEE Trans. Microw. Theory Tech.*, vol. 67, no. 10, pp. 4042–4054, Oct. 2019.
- [5] S. K. Dehkordi, L. Gaudio, M. Kobayashi, G. Caire, and G. Colavolpe, “Beam-space mimo radar for joint communication and sensing with OTFS modulation,” *IEEE Transactions on Wireless Communications*, pp. 1–1, 2023.
- [6] O. Kanhere, S. Goyal, M. Beluri, and T. S. Rappaport, “Target localization using bistatic and multistatic radar with 5g nr waveform,” in *2021 IEEE 93rd Vehicular Technology Conference (VTC2021-Spring)*. IEEE, 2021, pp. 1–7.
- [7] K. Abratkiewicz, A. Księżyk, M. Plotka, P. Samczyński, J. Wszolek, and T. P. Zielinski, “SSB-based signal processing for passive radar using a 5G network,” *IEEE Journal of Selected Topics in Applied Earth Observations and Remote Sensing*, vol. 16, pp. 3469–3484, 2023.
- [8] A. Schwind, C. Andrich, P. Wendland, M. Döbereiner, G. Del Galdo, G. Schaefer, R. S. Thomä, and M. A. Hein, “Bi-static delay-doppler emulation of cooperative passive vehicle-to-X radar,” in *2019 13th European Conference on Antennas and Propagation (EuCAP)*, 2019, pp. 1–5.
- [9] H. Zhang, N. Shlezinger, F. Guidi, D. Dardari, and Y. C. Eldar, “6g wireless communications: From far-field beam steering to near-field beam focusing,” *IEEE Communications Magazine*, vol. 61, no. 4, pp. 72–77, 2023.
- [10] Z. Wang, X. Mu, and Y. Liu, “Near-field integrated sensing and communications,” *IEEE Communications Letters*, vol. 27, no. 8, pp. 2048–2052, 2023.
- [11] Y. Liu, Z. Wang, J. Xu, C. Ouyang, X. Mu, and R. Schober, “Near-field communications: A tutorial review,” *IEEE Open Journal of the Communications Society*, pp. 1–1, 2023. [Online]. Available: <https://doi.org/10.1109/OJFocs.2023.3305583>

- [12] E. Björnson, O. T. Demir, and L. Sanguinetti, "A primer on near-field beamforming for arrays and reconfigurable intelligent surfaces," in *2021 55th Asilomar Conference on Signals, Systems, and Computers*, 2021, pp. 105–112.
- [13] H. Griffiths, "From a different perspective: principles, practice and potential of bistatic radar," in *2003 Proceedings of the International Conference on Radar (IEEE Cat. No.03EX695)*, 2003, pp. 1–7.
- [14] A. Sabharwal, P. Schniter, D. Guo, D. W. Bliss, S. Rangarajan, and R. Wichman, "In-band full-duplex wireless: Challenges and opportunities," *IEEE J. Sel. Areas Commun.*, vol. 32, no. 9, pp. 1637–1652, Sep. 2014.
- [15] M. Duarte and A. Sabharwal, "Full-duplex wireless communications using off-the-shelf radios: Feasibility and first results," in *2010 Conference Record of the Forty Fourth Asilomar Conference on Signals, Systems and Computers*, 2010, pp. 1558–1562.
- [16] J. A. Zhang, F. Liu, C. Masouros, R. W. Heath, Z. Feng, L. Zheng, and A. Petropulu, "An overview of signal processing techniques for joint communication and radar sensing," *IEEE Journal of Selected Topics in Signal Processing*, vol. 15, no. 6, pp. 1295–1315, 2021.
- [17] H. L. V. Trees, *Optimum Array Processing: Part IV of Detection, Estimation, and Modulation Theory*. John Wiley & Sons, Inc., 2002.
- [18] F. Sohrabi and W. Yu, "Hybrid digital and analog beamforming design for large-scale antenna arrays," *IEEE Journal of Selected Topics in Signal Processing*, vol. 10, no. 3, pp. 501–513, 2016.
- [19] 5G NR; *Physical layer procedures for data*, 3GPP TS 38.214, June 2023, v17.6.0 Release 17. [Online]. Available: <https://portal.3gpp.org/desktopmodules/Specifications/SpecificationDetails.aspx?specificationId=3216>
- [20] J. Wang, Z. Lan, C. woo Pyo, T. Baykas, C. sean Sum, M. Rahman, J. Gao, R. Funada, F. Kojima, H. Harada, and S. Kato, "Beam codebook based beamforming protocol for multi-gbps millimeter-wave wpan systems," *IEEE Journal on Selected Areas in Communications*, vol. 27, no. 8, pp. 1390–1399, 2009.
- [21] Z. Xiao, T. He, P. Xia, and X.-G. Xia, "Hierarchical codebook design for beamforming training in millimeter-wave communication," *IEEE Transactions on Wireless Communications*, vol. 15, no. 5, pp. 3380–3392, 2016.
- [22] S. K. Dehkordi, J. C. Hauffen, P. Jung, R. Hernangomez, G. Caire, and S. Stanczak, "Multi-scatter-point target estimation for sensing-assisted OTFS automotive communication," in *WSA & SCC 2023; 26th International ITG Workshop on Smart Antennas and 13th Conference on Systems, Communications, and Coding*, 2023, pp. 1–6.
- [23] W. Boyse and A. Seidl, "A hybrid finite element method for 3-d scattering using nodal and edge elements," *IEEE Transactions on Antennas and Propagation*, vol. 42, no. 10, pp. 1436–1442, 1994.
- [24] P. Kumari, J. Choi, N. González-Prelcic, and R. W. Heath, "IEEE 802.11ad-based radar: An approach to joint vehicular communication-radar system," *IEEE Trans. Veh. Technol.*, vol. 67, no. 4, pp. 3012–3027, April 2018.
- [25] D. H. N. Nguyen and R. W. Heath, "Delay and Doppler processing for multi-target detection with IEEE 802.11 OFDM signaling," in *Proc. IEEE Int. Conf. Acoustics, Speech, and Signal Processing (ICASSP)*, March 2017, pp. 3414–3418.
- [26] D. C. Rife and R. R. Boorstyn, "Multiple tone parameter estimation from discrete-time observations," *The Bell System Technical Journal*, vol. 55, no. 9, pp. 1389–1410, 1976.
- [27] H. V. Poor, *An Introduction to Signal Detection and Estimation (2nd Ed.)*. Berlin, Heidelberg: Springer-Verlag, 1994.
- [28] M. Kronauge and H. Rohling, "Fast two-dimensional cfar procedure," *IEEE Transactions on Aerospace and Electronic Systems*, vol. 49, no. 3, pp. 1817–1823, 2013.
- [29] L. Pucci, E. Matricardi, E. Paolini, W. Xu, and A. Giorgetti, "Performance analysis of a bistatic joint sensing and communication system," in *2022 IEEE International Conference on Communications Workshops (ICC Workshops)*, 2022, pp. 73–78.
- [30] N. J. Willis, *Bistatic radar*, 2nd ed. SciTech Publishing, 2005.
- [31] E. Björnson and L. Sanguinetti, "Power scaling laws and near-field behaviors of massive mimo and intelligent reflecting surfaces," *IEEE Open Journal of the Communications Society*, vol. 1, pp. 1306–1324, 2020.
- [32] F. Wang, X. Wang, X. Li, X. Hou, L. Chen, S. Suyama, and T. Asai, "Ring-type codebook design for reconfigurable intelligent surface near-field beamforming," in *2022 IEEE 33rd Annual International Symposium on Personal, Indoor and Mobile Radio Communications (PIMRC)*, 2022, pp. 391–396.
- [33] Z. Wang, X. Mu, and Y. Liu, "Near-field integrated sensing and communications," *IEEE Communications Letters*, pp. 1–1, 2023. [Online]. Available: <https://doi.org/10.1109%2Ftcomm.2023.3280132>
- [34] A. Antoniou and W.-S. Lu, "Design of two-dimensional digital filters by using the singular value decomposition," *IEEE Transactions on Circuits and Systems*, vol. 34, no. 10, pp. 1191–1198, 1987.
- [35] W.-S. Lu, "A unified approach for the design of 2-d digital filters via semidefinite programming," *IEEE Transactions on Circuits and Systems I: Fundamental Theory and Applications*, vol. 49, no. 6, pp. 814–826, 2002.
- [36] F. Wang, V. Balakrishnan, P. Zhou, J. Chen, R. Yang, and C. Frank, "Optimal array pattern synthesis using semidefinite programming," *IEEE Transactions on Signal Processing*, vol. 51, no. 5, pp. 1172–1183, 2003.
- [37] M. Goemans and D. Williamson, "Improved approximation algorithms for maximum cut and satisfiability problems using semidefinite programming," *Journal of Association for Computing Machinery*, no. 42(6), p. 1115–1145, 1995.
- [38] P. W. Kassakian, "Convex approximation and optimization with applications in magnitude filter design and radiation pattern synthesis," PhD dissertation, University of California, Berkeley, 2006.
- [39] V. S. Chernyak, *Fundamentals of multisite radar systems: multistatic radars and multistatic radar systems*. CRC press, 1998.
- [40] L. Scharf and C. Demeure, *Statistical Signal Processing: Detection, Estimation, and Time Series Analysis*, ser. Addison-Wesley series in electrical and computer engineering. Addison-Wesley Publishing Company, 1991. [Online]. Available: [https://books.google.de/books?id=y\\_dSAAAMAAJ](https://books.google.de/books?id=y_dSAAAMAAJ)